OPEN ACCESS



MIDIS: MIRI Uncovers Virgil, the First Little Red Dot with Clear Detection of Its Host Galaxy at $z \simeq 6.6$

```
Edoardo Iani<sup>1,2</sup>, Pierluigi Rinaldi<sup>1,3</sup>, Karina I. Caputi<sup>1,4</sup>, Marianna Annunziatella<sup>5</sup>, Danial Langeroodi<sup>6</sup>, Jens Melinder<sup>7</sup>, Pablo G. Pérez-González<sup>5</sup>, Javier Álvarez-Márquez<sup>5</sup>, Leindert A. Boogaard<sup>8,9</sup>, Sarah E. I. Bosman<sup>9,10</sup>, Luca Costantin<sup>5</sup>, Thibaud Moutard<sup>11</sup>, Luis Colina<sup>5</sup>, Göran Östlin<sup>7</sup>, Thomas R. Greve<sup>4,12,13</sup>, Gillian Wright<sup>14</sup>, Almudena Alonso-Herrero<sup>15</sup>, Arjan Bik<sup>7</sup>, Steven Gillman<sup>4,12</sup>, Alejandro Crespo Gómez<sup>5</sup>, Jens Hjorth<sup>16</sup>,
Sarah Kendrew<sup>17</sup>, Alvaro Labiano<sup>15,18</sup>, John P. Pye<sup>19</sup>, Tuomo V. Tikkanen<sup>19</sup>, Fabian Walter<sup>20</sup>, Manuel Güdel<sup>21,22</sup>, Thomas Henning<sup>20</sup>, and Paul P. van der Werf<sup>8</sup>
     <sup>1</sup> Kapteyn Astronomical Institute, University of Groningen, P.O. Box 800, 9700 AV Groningen, The Netherlands; edoardo.iani@ist.ac.at, iani@astro.rug.nl
                                               Institute of Science and Technology Austria (ISTA), Am Campus 1, 3400 Klosterneuburg, Austria
                                             3 Steward Observatory, University of Arizona, 933 North Cherry Avenue, Tucson, AZ 85721, USA Cosmic Dawn Center (DAWN), Copenhagen, Denmark
                                  <sup>5</sup> Centro de Astrobiología (CAB), CSIC-INTA, Ctra. de Ajalvir km 4, Torrejón de Ardoz, E-28850, Madrid, Spain
                                               DARK, Niels Bohr Institute, University of Copenhagen, Jagtvej 155, 2200 Copenhagen, Denmark
                       <sup>7</sup> Department of Astronomy, Stockholm University, Oscar Klein Centre, AlbaNova University Centre, 106 91 Stockholm, Sweden
                                                   <sup>8</sup> Leiden Observatory, Leiden University, P.O. Box 9513, 2300 RA Leiden, The Netherlands
                                                            Max Planck Institute for Astronomy, Königstuhl 17, 69117 Heidelberg, Germany
                                     <sup>10</sup> Institute for Theoretical Physics, Heidelberg University, Philosophenweg 12, D-69120, Heidelberg, Germany
   11 European Space Agency (ESA), European Space Astronomy Centre (ESAC), Camino Bajo del Castillo s/n, 28692 Villanueva de la Cañada, Madrid, Spain
                                             DTU Space, Technical University of Denmark, Elektrovei, Building 328, 2800, Kgs. Lyngby, Denmark
                                           Department of Physics and Astronomy, University College London, Gower Street, WC1E 6BT, UK
                                     <sup>14</sup> UK Astronomy Technology Centre, Royal Observatory Edinburgh, Blackford Hill, Edinburgh EH9 3HJ, UK
                       15 Centro de Astobiología (CAB), CSIC-INTA, Camino Bajo del Castillo s/n, E-28692 Villanueva de la Cañada, Madrid, Spain 16 DARK, Niels Bohr Institute, University of Copenhagen, Jagtvej 128, 2200 Copenhagen, Denmark
                17 European Space Agency (ESA), ESA Office, Space Telescope Science Institute, 3700 San Martin Drive, Baltimore, MD 21218, USA

18 Telespazio UK for the European Space Agency, ESAC, Camino Bajo del Castillo s/n, E-28692 Villanueva de la Cañada, Madrid, Spain

19 School of Physics & Astronomy, Space Park Leicester, University of Leicester, 92 Corporation Road, Leicester LE4 5SP, UK

20 Max-Planck-Institut für Astronomie, Königstuhl 17, 69117 Heidelberg, Germany

21 Description of Astronomic University of Vicence Tiblescope Park 17, A 1180 Vicence Aportice
                                             <sup>21</sup> Department of Astrophysics, University of Vienna, Türkenschanzstr. 17, A-1180 Vienna, Austria
                                   ETH Zürich, Institute for Particle Physics and Astrophysics, Wolfgang-Pauli-Str. 27, 8093 Zürich, Switzerland
                                               Received 2024 June 26; revised 2025 June 2; accepted 2025 June 12; published 2025 August 12
```

Abstract

We present Virgil, a Mid-Infrared Instrument (MIRI) extremely red object detected with the F1000W filter as part of the MIRI Deep Imaging Survey observations of the Hubble Ultra Deep Field. Virgil is an Ly α emitter (LAE) at $z_{\rm spec}=6.6312\pm0.0019$ (from the Very Large Telescope/MUSE) with a rest-frame UV-to-optical spectral energy distribution (SED) typical of LAEs at similar redshifts. However, MIRI observations reveal an unexpected extremely red color at rest-frame near-infrared (NIR) wavelengths, F444W – F1000W = 2.33 \pm 0.06. Such a steep rise in the NIR, completely missed without MIRI imaging, is poorly reproduced by models including only stellar populations and hints toward the presence of an active galactic nucleus, although alternative explanations such as extreme dust obscuration and strong nebular continuum and emission lines contribution due to young stellar ages cannot be completely ruled out. According to the shape of its overall SED, Virgil belongs to the recently discovered population of little red dots but displays an extended rest-frame UV-optical wavelength morphology following a 2D-Sérsic profile with an average index of $n=0.93^{+0.85}_{-0.31}$ and $r_e=0.49^{+0.05}_{-0.11}$ pkpc. Only at MIRI wavelengths, Virgil is unresolved due to the coarser point-spread function. This discovery demonstrates the crucial importance of deep MIRI surveys to reveal the true nature and properties of high-z galaxies that otherwise would be misinterpreted and raises the question of how common Virgil-like objects could be in the early Universe.

Unified Astronomy Thesaurus concepts: Galaxy formation (595); Galaxy evolution (594); High-redshift galaxies (734); Stellar populations (1622); Active galactic nuclei (16); Galaxy ages (576); James Webb Space Telescope (2291)

1. Introduction

Since the release of its first observations in 2022 July, JWST has opened a new window into the study of the early Universe (J. P. Gardner et al. 2023), both by giving us exceptional details on

Original content from this work may be used under the terms of the Creative Commons Attribution 4.0 licence. Any further distribution of this work must maintain attribution to the author(s) and the title of the work, journal citation and DOI.

known high-z sources (e.g., A. J. Bunker et al. 2023; L. Colina et al. 2023; R. Maiolino et al. 2024) and revealing the presence of new galaxies (e.g., H. Atek et al. 2023b, 2023a; C. M. Casey et al. 2023; B. E. Robertson et al. 2023), some of which are high-z (z > 10) candidates (e.g., E. Iani et al. 2022; G. Rodighiero et al. 2023; G. Gandolfi et al. 2025), while others are spectroscopically confirmed (e.g., A. J. Bunker et al. 2023; E. Curtis-Lake et al. 2023; B. Wang et al. 2023; M. Castellano et al. 2024).

Thanks to JWST, new galaxy populations have also been discovered, e.g., galaxies with very high equivalent width

emission lines (J. Álvarez-Márquez et al. 2024; P. Rinaldi et al. 2023; S. E. van Mierlo et al. 2024; K. Boyett et al. 2024) and the enigmatic class of the so-called "little red dots" (LRDs; e.g., G. Barro et al. 2024; I. Labbe et al. 2023; D. Langeroodi & J. Hjorth 2023a; V. Kokorev et al. 2024; J. Matthee et al. 2024; P. G. Pérez-González et al. 2024a), i.e., compact sources with distinct spectral energy distributions (SEDs) showing clear Lyman and Balmer breaks and a characteristic "v-shaped" SED (in the λ – f_{λ} plane) implying blue rest-frame UV-to-optical colors and red optical-to-infrared colors. Their nature is still under strong debate (e.g., I. Labbe et al. 2023; K. Inayoshi & K. Ichikawa 2024; Y. Li et al. 2024; J. Bellovary 2025).

In this context, the Mid-Infrared Instrument (MIRI; G. H. Rieke et al. 2015; G. S. Wright et al. 2015, 2023) on JWST, and in particular, its imager MIRIM (P. Bouchet et al. 2015; D. Dicken et al. 2024) is allowing us to unfold the intermediate/high-redshift Universe by enabling us to study galaxies in the wavelength range from 5.6 μ m through 25.5 μ m at an unprecedented spatial resolution and sensitivity (J. Rigby et al. 2023). Among its numerous results, MIRIM has been crucial in revealing previously undetected faint galaxies (e.g., H. B. Akins et al. 2023; G. Barro et al. 2024; A. Kirkpatrick et al. 2023; P. G. Pérez-González et al. 2024a), uncovering a large population of obscured active galactic nuclei (AGNs; e.g., G. Yang et al. 2023), and characterizing the physical properties of distant galaxies in great detail (e.g., J. Álvarez-Márquez et al. 2024; L. Colina et al. 2023), including their morphologies (e.g., L. A. Boogaard et al. 2024; L. Costantin et al. 2024; S. Gillman et al. 2024). MIRI also has a unique role in the study of early galaxies. By leveraging the deepest image of the Universe at 5.6 μ m (G. Östlin et al. 2025), P. Rinaldi et al. (2023) inferred for the first time the presence of H α emission in individual galaxies at $z \approx 7-9$ via broadband photometric excess.

Thanks to its capabilities, MIRIM holds the promise to reveal and constrain the rest-frame optical-near-infrared (NIR) properties of galaxies at z>2 and further push for the discovery and study of the class of "extremely red objects" (EROs; e.g., R. Elston et al. 1988; J. R. Graham & A. Dey 1996; K. I. Caputi et al. 2004), i.e., sources displaying a large (red) color between bands probing their rest-frame optical and NIR emission (e.g., R-K>5 in the Vega system, R. Elston et al. 1988). In this regard, particularly remarkable is the recent discovery of the first ERO detected thanks to MIRI imaging at 10 μ m by P. G. Pérez-González et al. (2024b): with a F444W – F1000W > 3.5 color, this object represented the first MIRI Extremely Red Object (MERO) reported in the era of JWST.

In this paper, we present and study Virgil, an MERO found in the MIRI Deep Imaging Survey (MIDIS; G. Östlin et al. 2025) F1000W imaging (α (J2000.0) = 03:32:37.9370 (hr); δ (J2000.0) = -27:47:10.712 (deg)). The source is clearly detected in the NIRCam bands, and it has already been cataloged in both the JWST Advanced Deep Extragalactic Survey (JADES) DR2 and Very Large Telescope (VLT)/MUSE catalogs (R. Bacon et al. 2023; M. J. Rieke et al. 2023b). Virgil is an Ly α emitter (LAE) at $z_{\rm spec}$ = 6.6312 \pm 0.0019, which shows an extremely red color between 4.4 and 10 μ m and is also red with respect to the bluest MIRI band (F560W), as revealed by MIDIS F560W imaging (G. Östlin et al. 2025). Without the MIRIM coverage, this unexpected

property of Virgil would have been completely missed, thus leaving us with a partial and biased knowledge of it.

This paper is organized as follows. In Section 2, we briefly describe the data sets used, and in particular, the MIDIS 10 μ m MIRI imaging and the ancillary Hubble Space Telescope (HST) and JWST NIRCam and MIRI observations. All the HST and JWST observations can be found in the Mikulski Archive for Space Telescopes (MAST²³), specifically the High Level Science Product repositories for the Hubble Legacy Fields (HLF; G. Illingworth 2015), JEMS (C. Williams et al. 2023), the JWST First Reionization Epoch Spectroscopically Complete Observations (FRESCO) Survey (P. Oesch & D. Magee 2023), and JADES (M. J. Rieke et al. 2023a). In addition, specific JWST data obtained for this project can be downloaded at these MAST data collection repositories: 10.17909/5txh-pj89 and 10.17909/bjk7-qh92. In Section 3, we describe the identification of Virgil, the assessment of its redshift, the decontamination of its light from the nearby LAE at $z \simeq 4.77$, the analysis of its morphology, and the extraction of its multiwavelength photometry. In Section 4, we discuss the possible nature and the importance of MIRI imaging for the detection and characterization of such an object. Finally, we summarize our findings and present our conclusions in

Throughout the paper, we assume a flat Λ CDM cosmology with $\Omega_M=0.3$, $\Omega_\Lambda=0.7$, and a Hubble constant of $H_0=70~{\rm km\,s^{-1}\,Mpc^{-1}}$. According to this cosmology, the luminosity distance of our target is $D_{\rm L}=64.8~{\rm Gpc}$, and the age of the Universe at its redshift was about 0.8 Gyr. We adopt the AB magnitudes (J. B. Oke & J. E. Gunn 1983). All stellar mass and star formation rate (SFR) estimations assume a universal Chabrier initial mass function (IMF; G. Chabrier 2003). Finally, unless otherwise stated, we report the average 5σ depth for pointlike sources of the available NIRCam and MIRI imaging of the MIDIS area as measured in circular apertures of r=0.0 (NIRCam) and r=0.0 (MIRI) as outlined by G. Östlin et al. (2025) and taking into account effects of pixel correlation as explained in A. S. Fruchter & R. N. Hook (2002). The depth estimates are not corrected for aperture.

2. Data Sets

2.1. MIRI F1000W Data

MIRI data in the F1000W filter were taken as part of MIDIS (PID: 1283; PI: G. Östlin; G. Östlin et al. 2025) in 2023 December. The observation consisted of 11 exposures, each with 100 groups and seven integrations, for a total on-source exposure time of 30.8 ks, centered on the Hubble Ultra Deep Field (HUDF; S. V. W. Beckwith et al. 2006). The dithering pattern was set to large-size cycling, with the 11 exposures taken in different positions on the sky separated by up to 10". This dithering pattern, with no repeated positions, was selected since it was found to be crucial for the detection of faint sources, such as Virgil, and their distinction from detector artifacts.

A detailed description of the reduction of the MIRI data is presented in P. G. Pérez-González et al. (2024b). Briefly, a super-background strategy is used to build background maps for every single image using all the other exposures (since they were taken during the same campaign), which results in a very homogeneous background (in terms of level and noise).

²³ https://mast.stsci.edu/portal/Mashup/Clients/Mast/Portal.html

Known sources are masked to avoid biasing the determination of the very local background in the super-background frame. Our final F1000W image, reduced with a 60 mas pixel scale, presents an average 5σ depth of 26.4 mag. We present the MIDIS F1000W data in Figure 1 (top panels) as the red channel of a red, green, blue (RGB) image built in combination with the NIRCam long-wavelength channels F277W and F356W.

2.2. Ancillary Data

We complement our MIRI observations at 10 μ m with a rich set of photometric and spectroscopic data publicly available. In particular, we extend our data set to include more MIRI observations, HST and JWST/NIRCam filters, the Atacama Large Millimeter/submillimeter Array (ALMA) surveys, and deep optical integral field spectroscopy by the Multi Unit Spectroscopic Explorer (MUSE) at VLT. We briefly summarize these ancillary data sets in the following sections.

2.2.1. Additional MIRI Data

We combine the recently acquired MIDIS F1000W data with the F560W ultra-deep observations also carried out by MIDIS in 2022 December and 2023 January. A thorough description of this data set is presented in G. Östlin et al. (2025). These observations consist of \sim 41 hr on source taken in the HUDF, reaching a 5σ depth of 28.6 mag. We add to the MIDIS observations the publicly available MIRI data gathered by the Systematic Mid-infrared Instrument Legacy Extragalactic Survey (SMILES; PID 1207; PI: G. Rieke; S. Alberts et al. 2024; J. Lyu et al. 2024; G. H. Rieke et al. 2024) in the F770W, F1280W, F1500W, F1800W, F2100W, and F2550W bands. We reduce the SMILES images following the same methodology applied to the MIDIS data set and obtain images with a 5σ depth of about 26.2 (F770W), 25.0 (F1280W), 24.9 (F1500W), 24.1 (F1800W), 23.6 (F2100W), and 21.8 (F2550W) mag, respectively.

2.2.2. NIRCam Data

We complement the MIRI data with NIRCam imaging taken by JADES (PIDs: 1180, 1210; P.I.: D. Eisenstein, N. Luetzgendorf; D. J. Eisenstein et al. 2023b), Data Release 2 (D. J. Eisenstein et al. 2023a), which includes also observations from the JWST Extragalactic Medium-band Survey (JEMS; PID: 1963; PIs: C. C. Williams, S. Tacchella, M. Maseda; C. C. Williams et al. 2023) and FRESCO (PID: 1895; PI: P. Oesch; P. A. Oesch et al. 2023). This data set provides a total of 14 bands from 0.9 to 4.8 μ m (F090W, F115W, F150W, F182M, F200W, F210M, F277W, F335M, F356W, F410M, F430M, F444W, F460M, F480M) with 5σ depths ranging from 30.5 to 30.9 mag.

2.2.3. HST Data

We obtain all the HST images over the HUDF from Hubble Legacy Field GOODS-S (HLF-GOODS-S; K. E. Whitaker et al. 2019). HLF-GOODS-S provides 13 HST bands covering a wide range of wavelengths (0.2–1.6 μ m), from the UV (WFC3/ UVIS F225W, F275W, and F336W filters), optical (Advanced Camera for Surveys/Wide Field Camera (ACS/WFC) F435W, F606W, F775W, F814W, and F850LP filters) to the NIR (WFC3/IR F098M, F105W, F125W, F140W,

and F160W filters). In this paper, we only made use of the deepest ones (i.e., F435W, F606W, F775W, F814W, F850LP, F105W, F125W, F140W, F160W). We refer the reader to K. E. Whitaker et al. (2019) for more detailed information on these observations.²⁴

2.2.4. MUSE Data

The HUDF has been extensively studied with MUSE (R. Bacon et al. 2010) at VLT as part of the MOSAIC and UDF-10 fields (GTO programs 094.A-0289(B), 095.A-0010 (A), 096.A-0045(A), and 096.A-0045(B), PI: R. Bacon) and the most recent MXDF observations (GTO Large Program 1101.A-0127, PI: R. Bacon). These observations cover a spectral wavelength range between 4750 and 9350 Å with a spectral resolving power (R) that varies from 1770 (4800 Å) to 3590 (9300 Å) and have a point-spread function (PSF; at 7750 Å), which can be described by a Moffat function (A. F. J. Moffat 1969) that varies from FWHM = 0.45 and $\beta = 1.89$ (MXDF), to FWHM = 0.460 and $\beta = 2.80$ (UDF-10), and to FWHM = 0.63 and β = 2.80 (MOSAIC), see R. Bacon et al. (2023) and their Table 4. In the MIDIS area, these observations have exceeded total exposure times of 140 hr, although the distribution of the depth in flux is not uniform across the whole area. More details about the HUDF MUSE surveys can be found in R. Bacon et al. (2017, 2023). In our study, we use the fully reduced MUSE data cubes for the MOSAIC + UDF-10 and MXDF programs, as well as the catalog of detected sources and corresponding redshifts presented in R. Bacon et al. (2023).²⁵

2.2.5. ALMA Data

The ALMA Spectroscopic Survey in the HUDF (ASPECS) is a Cycle 4 Large Program over a 4.6 arcmin² scan at 1.2 mm (band 6; R. Decarli et al. 2020; J. González-López et al. 2020) and 3.0 mm (band 3; R. Decarli et al. 2019; J. González-López et al. 2019). The ultra-deep 1.2 mm data reaches an rms sensitivity of 9.3 μ Jy beam⁻¹, with beam dimensions of 1".5 × 1".1. The 3.0 mm data reaches 1.4 μ Jy beam⁻¹, with a 1".8 × 1".5 beam. We download the fully reduced ALMA images from the official ASPECS website. 26

3. Selection and Properties of the MERO Virgil

In this paper, we present Virgil ($\alpha(J2000.0) = 03:32:37.9370$ (hr); $\delta(J2000.0) = -27:47:10.712$ (deg)), a source in the deep MIDIS F1000W image of the HUDF, which is counterpart to an LAE at z = 6.6312 from MUSE/VLT (Section 3.2). Despite being already known from shorter wavelength data (R. Bacon et al. 2023; D. J. Eisenstein et al. 2023a; M. J. Rieke et al. 2023), new important insights into the nature of this object come from the new deep MIRI observations at $10~\mu m$. In particular, Virgil displays an extreme F444W – F1000W red color ($\geqslant 2$) that classifies it as an ERO. Since the ERO nature of this source can only be determined with MIRI, we refer to it as MERO.

²⁴ The HLF-GOODS-S imaging is available at https://archive.stsci.edu/prepds/hlf/.

²⁵ The MUSE cubes can be obtained at https://amused.univ-lyon1.fr/project/UDF/.

²⁶ The ASPECS images are available at https://almascience.org/alma-data/

The ASPECS images are available at https://almascience.org/alma-data/lp/ASPECS.

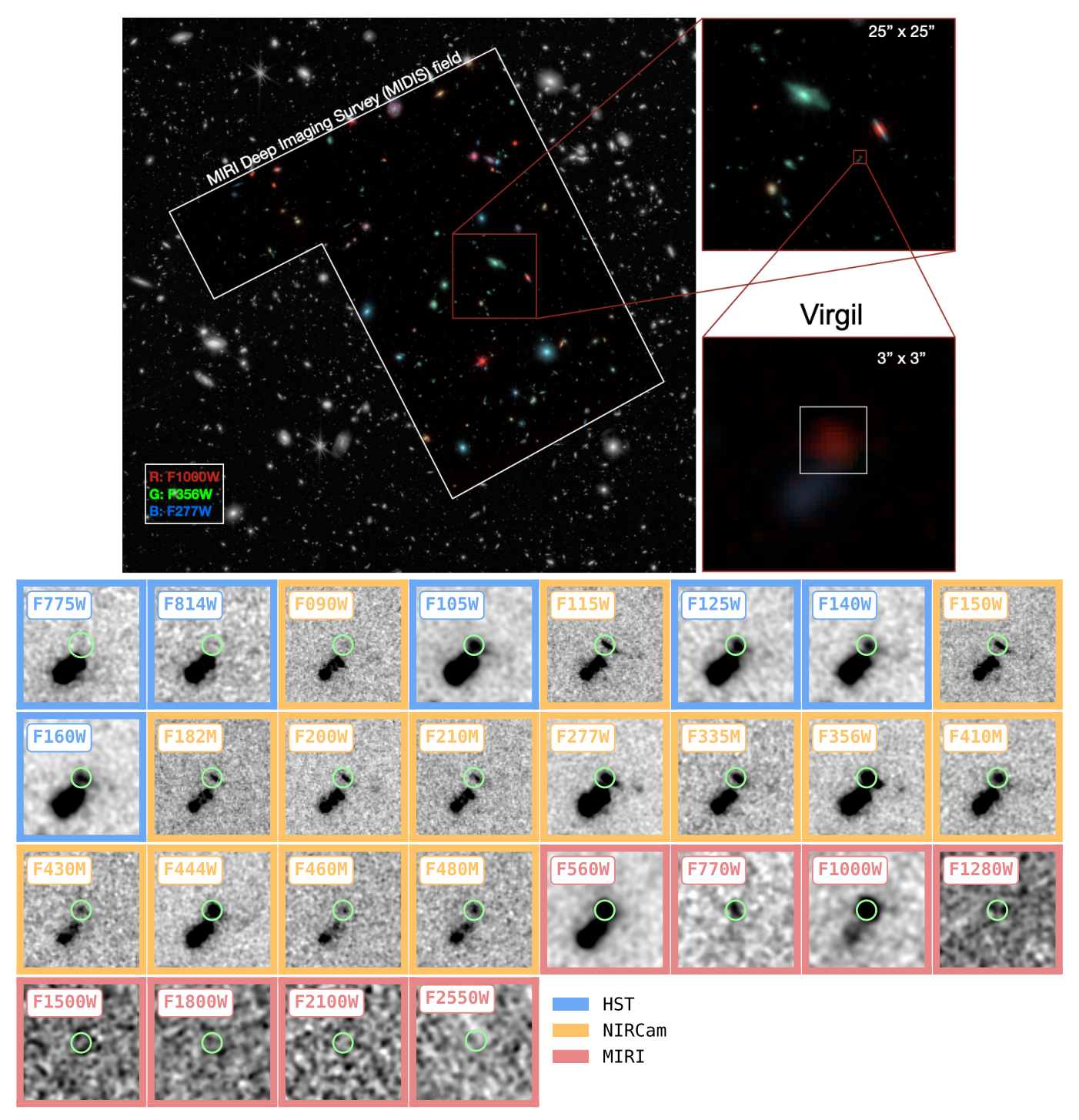


Figure 1. Top panel: RGB composition of the MIDIS field. The color images have been built with JADES data in two NIRCam filters, F277W and F356W, and the MIDIS MIRI F1000W filter (all convolved to the same PSF as MIRI/F1000W). In the background, we show the HUDF JADES data in gray scale. We show a series of zoomed-in RGB frames that lead to the MERO source, Virgil (α (J2000.0) = 03:32:37.9370 (hr); δ (J2000.0) = -27:47:10.712 (deg)). The Virgil object is highlighted with a square in the RGB frame at the bottom right. Bottom panel: cutouts (2".5 × 2".5) of Virgil from HST/ACS and WFC3 (F775W, F814W, F105W, F125W, F140W, and F160W), JWST/NIRCam (F090W, F115W, F150W, F200W, F210M, F277W, F335M, F356W, F410M, F430M, F444W, F460M, and F480M) and JWST/MIRI (F560W, F770W, F1000W, F1280W, F1500W, F1800W, F2100W, and F2550W). We highlight Virgil with a green circle (r = 0".2.) HST cutouts below 0.7 μ m are not shown here.

3.1. Identification of the MERO Virgil

Motivated by the recently reported discovery of the MERO Cerberus found in the MIDIS field (F444W - F1000W > 3.5; P. G. Pérez-González et al. 2024b), we decided to further scout the MIDIS area to discover additional MIRI red objects. To do

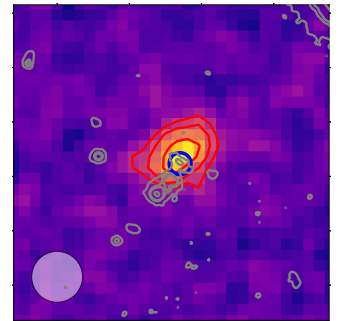
so, we make use of the SEXTRACTOR software (E. Bertin & S. Arnouts 1996) directly using the MIRI/F1000W map as detection image. We follow the hot-mode extraction described in A. Galametz et al. (2013), which is particularly effective for detecting extremely faint sources and constructing a photometric MIRI/F1000W catalog based on the SEXTRACTOR

magnitude estimates MAG_AUTO. We crossmatch our catalog (using a 0".2 search radius) to the official JADES DR2 catalog published by D. J. Eisenstein et al. (2023a) to only consider those sources showing a red F444W – F1000W color (F444W – F1000W \geqslant 1.5) and a robust F1000W detection signal-to-noise ratio (S/N \geqslant 5). The reddest object we find in our sample displays a F444W – F1000W = 2.33 \pm 0.06. We name this MERO Virgil, to acknowledge the fact that it is very close in projection to Cerberus (separation $\delta\approx$ 2".3). An RGB image of the source built with NIRCam and MIRI data is presented in the top right panel of Figure 1, together with a series of postage stamps showing Virgil from 0.7 to 21 μm .

3.2. Redshift Assessment of Virgil

In the JADES DR2 catalog (D. J. Eisenstein et al. 2023b), Virgil is listed with ID 206038 and a photometric redshift of $z_{\rm phot} \approx 6.62$. This redshift estimate agrees with the fact that our source appears to be a NIRCam F090W dropout, see the cutouts presented in Figure 1.

However, to better constrain the properties of our target, we investigate if we can derive a spectroscopic redshift z_{spec} from the available MUSE observations. In fact, based on the z_{phot} reported by the JADES DR2 catalog, the MUSE data should cover Virgil's rest-frame UV emission. Therefore, we look for the possible presence of emission lines, and in particular, of the Ly α line in the MUSE cube. To do so, we extract the MUSE 1D spectrum at the coordinates of our target within circular apertures of different sizes (r = 0.4, 0.8). Despite being strongly contaminated by the extended rest-frame UV emission of a close-by LAE at $z_{\rm spec} \simeq 4.77$ (ID 53; R. Bacon et al. 2023), in the MUSE 1D spectrum, we find a spectral feature appearing only at the position of the MERO. This line cannot be explained by any known emission line in the UV spectrum of galaxies at z = 4.77 and falls at the expected wavelength of the Ly α at $z \simeq 6.63$ (i.e., ≈ 9280 Å, see the right panel of Figure 2). The classification of this spectral feature as Virgil's Ly α is in agreement with the publicly available catalog of MUSE-detected sources by R. Bacon et al. (2023). Particularly, R. Bacon et al. (2023) list this source (ID 7699) as an LAE at a spectroscopic redshift $z_{\rm spec} = 6.6312 \pm 0.0019$ (quality_flag = 2, i.e., good confidence²⁷) with an Ly α flux $F(\text{Ly}\alpha) \approx 1.6 \times 10^{-18} \, \text{erg s}^{-1} \, \text{cm}^{-2}$ (corresponding to an Ly α luminosity $L(\text{Ly}a) \approx 8.1 \times 10^{41} \, \text{erg s}^{-1}$) and S/N ≈ 8 . Therefore, we assume $z_{\rm spec} = 6.6312 \pm 0.0019$ as Virgil's redshift for the rest of our analysis. Nonetheless, given the wealth of recent spectroscopic campaigns in the HUDF, we also verify if our target had been observed by FRESCO (PID: 1895; PI: P. Oesch, P. A. Oesch et al. 2023), NGDEEP (PID: 2079; PI: Finkelstein, M. B. Bagley et al. 2024), and JADES surveys. Unfortunately, our target is not detected in FRESCO's NIRCam Wide Field Slitless Spectroscopy (WFSS) observations,²⁸ nor in NGDEEP's NIRISS WFSS observations.² Finally, the NIRSpec Micro Shutter Array (MSA) observations



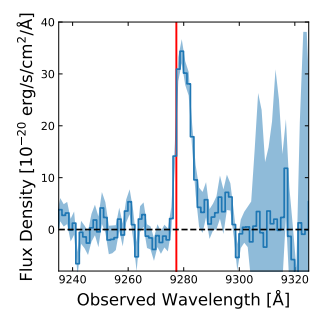


Figure 2. Left panel: MUSE pseudo-narrowband image $(6'' \times 6'')$ of Virgil's Ly α emission. Red contours are drawn at 2σ , 3σ , and 5σ , while gray contours are representative of the JWST/NIRCam F200W imaging. The source position is indicated with a 0.2 radius circle. The MUSE PSF is shown in the bottom left corner. Right panel: MUSE 1D spectrum of Virgil's Ly α . The vertical red line is indicative of the expected position of the Ly α at z = 6.6312.

from JADES (F. D'Eugenio et al. 2025) in HUDF did not cover the area of our target.

3.3. Removal of Virgil's Contaminant

In the JADES DR2 catalog, Virgil's contaminant at $z \approx 4.77$ (R. Bacon et al. 2023; see also J. Matthee et al. 2022) turns out to be constituted by two sources: ID 285736 and ID 206035. With respect to Virgil's location, ID 285736 is about 0".4 away while ID 206035 has a separation of 0".7 both in the southeast direction. To avoid the contamination of Virgil's photometry due to this extended lower redshift LAE, we model and subtract its contribution at all wavelengths. To do so, we resort to the galaxy morphology modeling tool ASTROPHOT (C. J. Stone et al. 2023). With ASTROPHOT, we model ID 285736 and ID 206035 with single Sérsic profiles while masking Virgil. From the first results, we find that to improve the quality of the residuals in several filters, it is necessary to introduce an optional third Sérsic component between ID 285736 and ID 206035, see also J. Matthee et al. (2022). In Figure 3, we present the residuals of the bestfit models obtained with ASTROPHOT for some of the available NIRCam and MIRI filters.

3.4. Virgil's Morphology

After the removal of Virgil's contaminant and before extracting its photometry (see Section 3.3), we briefly investigate Virgil's morphology.

At NIRCam wavelengths our target is clearly elongated in the southwest direction and features a tail that seems to end up in a (faint) clump (Beatrix; $\alpha(J2000.0) = 03:32:37.8844$ (hr); $\delta(J2000.0) = -27:47:10.979$) that can be detected at several NIRCam wavelengths but is completely missing in the MIRI imaging, see Figure 3. On the basis of the current data, it is difficult to assess whether Beatrix is a clump of Virgil or a different object at a different redshift (see Section 3.5). However, if confirmed at Virgil's redshift, the separation between Virgil and Beatrix ($\delta \approx 0.75$) would correspond to a projected distance of about 4 pkpc, and considering its pointlike nature, a size of $r \lesssim 0.96 \simeq 0.3$ pkpc.

After masking Beatrix and other close-by sources, the extracted surface brightness (SB) profile shows that Virgil is an extended object at wavelengths $\lambda < 7~\mu m$, while at 7.7 and $10~\mu m$, it is unresolved due to the coarser MIRI PSF. This is

 $^{^{\}overline{27}}$ An LAE with <code>quality_flag = 2</code> has an Ly\$\alpha\$ S/N > 5 and a width and asymmetry compatible with typical Ly\$\alpha\$ line shapes (R. Bacon et al. 2023). 28 The FRESCO line sensitivity (estimated for compact sources and integrated over the full extent of the line) is $\approx 2 \times 10^{-18}$ erg s $^{-1}$ cm $^{-2}$ at 5\$\sigma\$ (P. A. Oesch

²⁹ The NGDEEP spectroscopy was carried out in the F115W, F150W, and F200W filters, reaching 5σ integrated emission-line limits of 1.2, 1.3, and 1.5×10^{-18} erg s⁻¹ cm², respectively (M. B. Bagley et al. 2024).

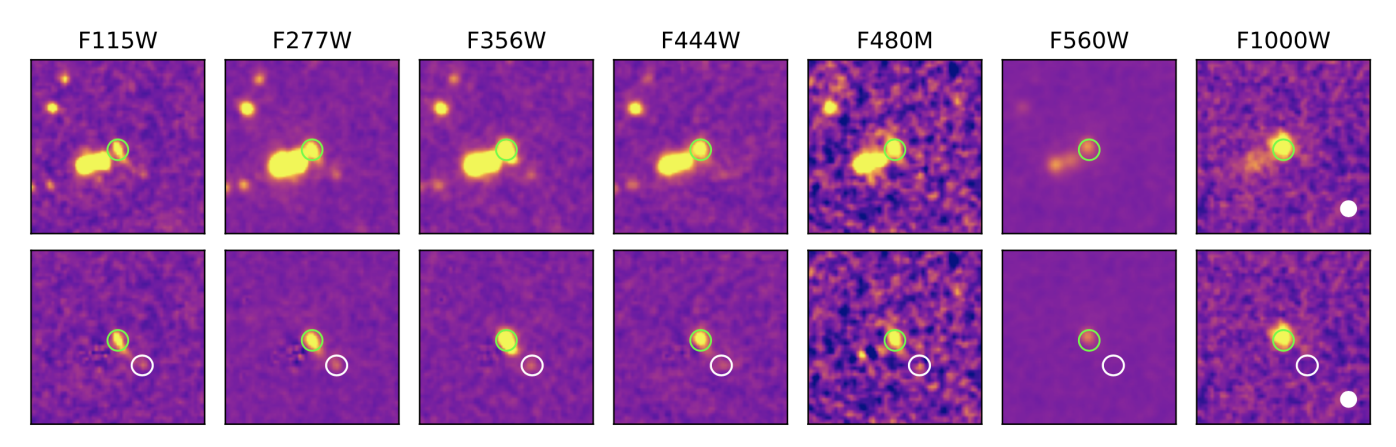


Figure 3. Top panels: cutouts (3.4 \times 3.4) of Virgil from NIRCam (F115W, F277W, F356W, F444W, F480M) and MIRI (F560W, F1000W) imaging. We highlight the position of Virgil with a green circle (0.2 radius). The southeastern component that gets dimmer at longer wavelengths is the LAE contaminant at z=4.77 (J. Matthee et al. 2022; R. Bacon et al. 2023). The white circle at the bottom right corner of the F1000W cutouts is representative of the MIRI 10 μ m PSF (FWHM \simeq 0.433). Bottom panels: same cutouts after modeling and subtracting the contaminant at z=4.77 and close-by sources. The white circle (0.42 radius) highlights the position of Beatrix.

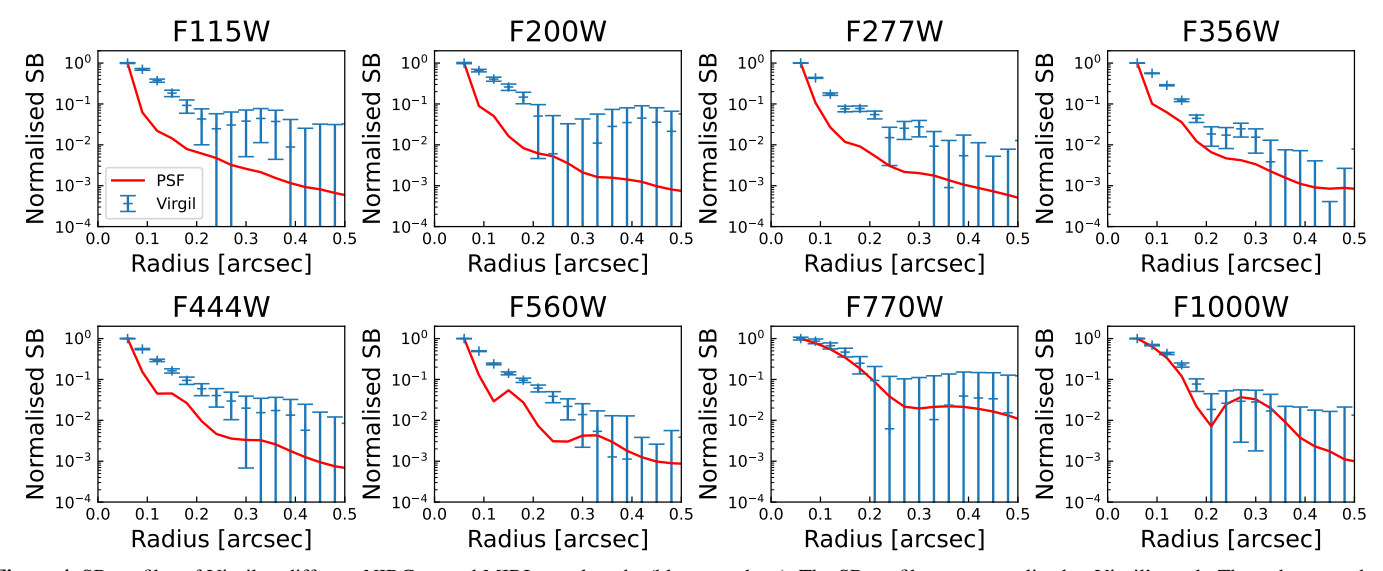


Figure 4. SB profiles of Virgil at different NIRCam and MIRI wavelengths (blue error bars). The SB profiles are normalized at Virgil's peak. The red curves show the JWST PSF trend for the different instruments and filters.

confirmed by the extraction of Virgil's radial SB profile and its comparison with the PSF trend in the different NIRCam and MIRI filters, see Figure 4.

If we fit a Sérsic profile (J. L. Sérsic 1963) to the SB radial profiles of the different broadband NIRCam and MIRI filters covering Virgil's rest-frame optical emission (i.e., F200W, F277W, F444W, F560W), we find a median value of the Sérsic index $n=0.93^{+0.85}_{-0.31}$ (16th and 84th percentiles) and an effective radius $r_e\simeq 0.09^{+0.01}_{-0.02}=0.49^{+0.05}_{-0.11}$ pkpc (16th and 84th percentiles). Both parameters are in agreement with the expected values of galaxy sizes and Sérsic indices at $z\simeq 6$ (W. Sun et al. 2024).

3.5. Extraction of Virgil's Photometry

After having removed the lower redshift interloper from all the 31 available HST (ACS and WFC3) and JWST (NIRCam and MIRI) bands, we extract Virgil's photometry in the wavelength range of $0.4-25 \,\mu \text{m}$ with SEP (K. Barbary et al. 2017), a PYTHON version of SEXTRACTOR (E. Bertin & S. Arnouts 1996). However, at the longest MIRI wavelengths

(>15 μ m), the available imaging is too shallow to detect Virgil. Also, after stacking together all the different MIRI bands available above 15 μ m (i.e., F1800W, F2100W, F2550W), we fail to detect our target. Hence, above 15 μ m, we make use of the 3σ upper limits on the flux density.

We extract Virgil photometry $\leq 15 \, \mu \mathrm{m}$ within Kron apertures (R. G. Kron 1980), allowing the Kron parameters to vary from filter to filter and replicating standard SEXTRACTOR settings, i.e., K=2.5 and a minimum radius r=1.75. Then, we correct the extracted fluxes to account for the missing flux outside the Kron aperture. To do so, we compute the fraction of the missing light outside the Kron apertures (e.g., K. E. Whitaker et al. 2011; J. R. Weaver et al. 2023; V. Kokorev et al. 2024) in comparison to the curve of growth of the different PSFs. For the JWST filters, we employ the PSF models by WEBBPSF (M. D. Perrin et al. 2014), while for HST, we resort to the curve of encircled energy reported by STScI. 30 We finally correct for Galactic extinction. Following

³⁰ The encircled energy curves are available at https://www.stsci.edu/hst/instrumentation/.

Table 1Photometry of Virgil

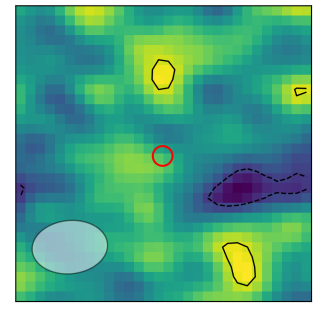
Instrument	Filter	$f_ u$	$\operatorname{err}(f_{\nu})$
		(nJy)	(nJy)
JWST/NIRCam	F090W	12.86	2.25
HST/ACS_WFC	F850LP	3.38	2.70
HST/WFC3_IR	F105W	22.07	1.95
JWST/NIRCam	F115W	30.54	2.00
HST/WFC3_IR	F125W	27.06	2.51
HST/WFC3_IR	F140W	22.90	2.59
JWST/NIRCam	F150W	28.92	1.85
HST/WFC3_IR	F160W	28.52	2.82
JWST/NIRCam	F182M	24.63	2.65
JWST/NIRCam	F200W	30.32	2.04
JWST/NIRCam	F210M	36.70	3.10
JWST/NIRCam	F277W	40.11	1.85
JWST/NIRCam	F335M	38.88	2.26
JWST/NIRCam	F356W	93.84	4.32
JWST/NIRCam	F410M	37.01	1.89
JWST/NIRCam	F430M	37.79	4.80
JWST/NIRCam	F444W	49.33	2.27
JWST/NIRCam	F460M	46.99	6.25
JWST/NIRCam	F480M	67.58	7.91
JWST/MIRI	F560W	107.70	3.03
JWST/MIRI	F770W	248.20	30.13
JWST/MIRI	F1000W	399.10	23.79
JWST/MIRI	F1280W	382.70	161.10
JWST/MIRI	F1500W	379.50	296.20

Note. In the above table, we report the photometry of Virgil as extracted after the modeling of the z = 4.77 LAE contaminant (see Section 3.3). The table is limited to only those bands where it was possible to detect Virgil.

E. Iani et al. (2024), we obtain the Galactic extinction corrections assuming the color excess reported on the IRSA webpage³¹ at Virgil's coordinates (E(B-V)=0.008, E. F. Schlafly & D. P. Finkbeiner 2011), and for all filters with an effective wavelength $\lambda_{\rm eff}<1.25~\mu{\rm m}$, applying the E. L. Fitzpatrick (1999) extinction law, while at longer wavelengths ($1.25 \leqslant \lambda_{\rm eff} < 8~\mu{\rm m}$), resorting to the R. Indebetouw et al. (2005) law. The correction factors for Galactic extinction are, however, quite negligible (<3%).

As in the case of SEXTRACTOR (S. Sonnett et al. 2013), SEP tends to underestimate the errors on the fluxes. To derive more reliable errors, we estimate them by drawing in each filter 1000 random Kron apertures on the sky region around Virgil $(6'' \times 6'')$ and, after having masked all the close-by sources, measuring their fluxes. We then take the standard deviation of all the different measurements, taking into account effects of pixel correlation (A. S. Fruchter & R. N. Hook 2002). Similarly to the fluxes, we also correct the errors to the total flux and Galactic extinction. Finally, we impose as a minimum error on the photometry a value of 0.05 mag for all bands. We present Virgil's photometry in Table 1.

In addition to HST and JWST imaging, we search for the detection of Virgil at (sub-)millimeter wavelengths, leveraging the available deep ASPECS ALMA dust continuum imaging at 1.2 and 3.0 mm. By carefully inspecting these maps, Virgil is not detected at either wavelength, see Figure 5. This finding implies 3σ upper limits on the flux density at 1.2 mm and 3.0 mm of 27.9 μ Jy and 4.2 μ Jy, respectively (assuming it is



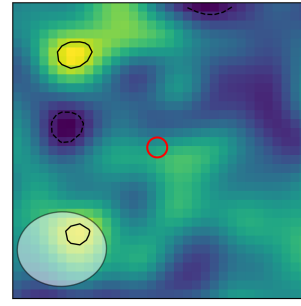


Figure 5. ALMA cutouts $(6'' \times 6'')$ at 1.2 mm (band 6) and 3.0 mm (band 3) from ASPECS. Contours are drawn at 1σ intervals starting at $\pm 2\sigma$ (dashed lines show negative contours). The source position is indicated with a 0''.2 radius circle. The beam size is shown in the bottom left corner. The source is not detected at either wavelength.

an unresolved pointlike source; L. A. Boogaard et al. 2024; P. G. Pérez-González et al. 2024b).

To assess the quality of our photometry on the images cleaned for the contaminant, we decided to test if, by running SED fitting codes on our photometry, we retrieve photometric redshifts in agreement with the spectroscopic redshift from MUSE. To this purpose, we employ both EAZY (G. B. Brammer et al. 2008) and CIGALE (D. Burgarella et al. 2005; S. Noll et al. 2009; M. Boquien et al. 2019). For EAZY, we adopt the v1.3 templates, which include a dusty galaxy with a high equivalent width emission-line spectrum, as well as new models for LRDs and high-redshift AGN+torus recently added based on JWST data (M. Killi et al. 2024). We do not impose any prior and work with minimum χ^2 photometric redshift estimates in the redshift range z = 0–20 and consider Virgil's photometry up to $10 \, \mu \text{m}$. For CIGALE, we run it only considering stellar templates and HST + JWST/NIRCam photometry, thus excluding the red upturn of our target's photometry. We use the same setting as presented in Section 3.7. According to both codes, the probability distribution of the photometric redshifts (PDZ) is uniquely determined (one single narrow peak) to be at 6.61 \pm 0.02 (EAZY) and 6.68 \pm 0.23 (CIGALE). Overall, we find a very good agreement with the spectroscopic estimate from MUSE.

In addition to Virgil, we extract the photometry for Beatrix following the same methodology as presented above. Our aim is to understand if we can assess the redshift of this object and discern if it is part of Virgil (clump) or a source at a different redshift. Due to the faintness of the source, however, we can only detect Beatrix in a few HST and JWST/NIRCam bands. On the derived photometry, we run both EAZY and CIGALE. Both codes return a multi-peaked PDZ. Interestingly, one of the peaks falls at Virgil's redshift and another one corresponds to the redshift of the contaminant LAE at $z \simeq 4.77$. The other peaks, however, suggest even lower redshift solutions ($z_{\rm phot} < 2$). Due to the limited data set available and the fact that we are not sure about its redshift, we do not further investigate this object.

3.6. Possible Galaxy-Galaxy Lensing Effect on Virgil

Due to the closeness of the contaminant to Virgil and the extended and stretched morphology of our target, we investigate whether Virgil could be affected by a galaxy-galaxy lensing effect (e.g., J. Matthee et al. 2017). To estimate the magnification of Virgil by the foreground LAE, we resort

³¹ https://irsa.ipac.caltech.edu/applications/DUST/

to the usage of the LENSTRONOMY software (S. Birrer & A. Amara 2018). The measured stellar masses of the two components of the foreground LAE are $M_{\star} \simeq 10^{8.3} M_{\odot}$ and $10^{8.6} M_{\odot}$ (D. J. Eisenstein et al. 2023b) for the objects located 0.4 and 0.7 from Virgil, respectively. The two components are located 0.732, or about 2.1 pkpc from each other at z = 4.77. The separations involved are sufficiently large that the lensing model is mostly unaffected by assumptions on the mass profile of the lensing galaxies; the Einstein radius is \sim 5 mas using a point-mass approximation, and $\lesssim 20 \,\mathrm{mas}$ when assuming extended mass distributions (maximized using an ellipsoid configuration). This configuration results in a magnification <5% of Virgil even under extreme assumptions for the total mass-to-stellar-mass ratios of 10 for both foreground galaxies. Due to the minimum value of the retrieved magnification, we do not consider corrections for lensing in the following analysis.

3.7. SED Analysis of Virgil

After having extracted its decontaminated photometry, we try to reproduce Virgil's observed SED with different SED-fitting codes, namely, CIGALE, BAGPIPES (A. C. Carnall et al. 2018), PROSPECTOR (B. D. Johnson et al. 2021), and SYNTHESIZER-AGN (P. G. Pérez-González et al. 2003, 2008, 2024a). Due to Virgil's red F444W – F1000W color, we decide to run the codes both excluding and considering the presence of an AGN (see Section 4). For the SED fitting, we consider all the photometry available, including the ALMA upper limits at 1.2 and 3 mm.

We first employ CIGALE, assuming a delayed exponentially declining star formation history (SFH; delayed- τ model) modeled with two stellar populations. We adopt the G. Bruzual & S. Charlot (2003, hereafter BC03) stellar populations models with both solar and subsolar metallicity ($Z = 0.2Z_{\odot}$), and the Chabrier IMF. We include nebular continuum and emission lines using solar and subsolar metallicity and allowing the electron density n_e and ionization parameter U to assume values of $n_e = 10, 100, 1000 \,\mathrm{cm}^{-3}$, and $\log_{10}(U) = -2, -1$, respectively. For the dust attenuation, we adopt D. Calzetti et al. (2000, hereafter C00), while for the far-infrared (FIR) emission, we resort to the B. T. Draine et al. (2014) models. We add the AGN emission using the SKIRTOR models (M. Stalevski et al. 2012, 2016) following the initial parameters suggested by G. Yang et al. (2023) but allowing for the presence of both a Type I (unobscured) and Type II (obscured) AGN.

As a second SED-fitting code, we run BAGPIPES, a stellar population synthesis modeling package built on the BC03 spectral library with the 2016 version of the MILES library (J. Falcón-Barroso et al. 2011). The code uses a P. Kroupa (2001) IMF, adopts the C00 dust attenuation curve, and includes nebular emission lines. The ionization parameter $\log_{10}(U)$ is set to vary between (-4, -2). The SFH is set to a two-component delayed- τ model, and we included an AGN component as in A. C. Carnall et al. (2023).

For PROSPECTOR, we adopt the setup described in detail in D. Langeroodi et al. (2023) and D. Langeroodi & J. Hjorth (2023b). In brief, we use five temporal bins to model the SFH nonparametrically while applying the continuity prior from J. Leja et al. (2019). The nebular emission is modeled using the CLOUDY (M. Chatzikos et al. 2023) templates compiled in N. Byler et al. (2017), while the gas-phase metallicity, stellar metallicity, and ionization parameters are modeled as free

parameters. We model the dust attenuation using the two-component model of M. Kriek & C. Conroy (2013), where one component affects the entire galaxy and the other models the additional reddening at the birthplace of young stars.

Finally, we run SYNTHESIZER-AGN. The code assumes that the SED can be modeled with a composite stellar population (P. G. Pérez-González et al. 2003, 2008) and AGN emission coming from the accretion disk and the dusty torus (P. G. Pérez-González et al. 2024a). The stellar emission includes a young and a more evolved star formation event, each one described by a delayed exponential function with timescales between 1 Myr and 1 Gyr, and with ages from 1 Myr up to the age of the Universe at the redshift of the source. The attenuation of the emission from each stellar population is independent and described by the C00 law, with A(V) values ranging from 0 to 10 mag for each population, considered to have completely independent attenuation. The stellar emission is described by the BC03 models, assuming a Chabrier IMF with stellar mass limits between 0.1 and $100 M_{\odot}$, and the nebular emission is also considered (P. G. Pérez-González et al. 2003). The AGN emission is modeled with a QSO average spectrum (D. E. Vanden Berk et al. 2001; E. Glikman et al. 2006). The dust emission from the AGN is modeled with the self-consistent templates of AGN tori presented in R. Siebenmorgen et al. (2015).

We present and discuss the results derived from the different SED-fitting codes in Section 4.

4. Discussion

4.1. Virgil's Properties without MIRI

As a first step, we decide to investigate Virgil's properties based only on its HST and JWST/NIRCam photometry, i.e., limiting our study to wavelengths $<5 \mu m$.

The SED of Virgil reveals a rest-frame blue UV continuum. Following M. Castellano et al. (2012), by fitting a power law to the observed fluxes ($f_{\lambda} \propto \lambda^{\beta_{\text{UV}}+2}$), we estimate a UV continuum slope of $\beta_{\text{UV}} = -2.1 \pm 0.3$ and an absolute UV magnitude at $1500 \,\text{Å}\,M(\text{UV}) = -19.1 \pm 0.1$ mag. Both parameters are well in agreement with what was recently found for other LAEs at similar redshifts (E. Iani et al. 2024) and suggest negligible effects due to dust extinction ($A_{1500} < 0.3 \, \text{mag}$; e.g., G. R. Meurer et al. 1999). If we convert the M(UV) into SFR following the prescription by R. C. Kennicutt & N. J. Evans (2012), we find an SFR(UV) $\simeq 1.7 \, M_{\odot} \, \text{yr}^{-1}$ (not corrected for dust extinction).

At optical wavelengths, Virgil's SED is characterized by a clear photometric excess in the F356W band (F335M - F356W = 0.96 \pm 0.08). Due to Virgil's redshift (i.e., $z_{\rm spec} = 6.6312 \pm$ 0.0019), this excess can be explained as the direct consequence of a strong H β + [O III] $\lambda\lambda$ 4959, 5007 ([O III], hereafter) emissionline complex entering the F356W filter. If we assume the continuum below $H\beta + [O III]$ as the average value between the F356W adjoining filters F335M and F410M and apply the prescriptions by E. Mármol-Queraltó et al. (2016), we can convert the photometric excess in F356W into the rest-frame equivalent width EW₀ of the line complex. From our photometry, we estimate EW₀(H β + [O III]) \approx 560 Å. This value is in good agreement with recent literature for emitters at $z \gtrsim 6$ (R. Endsley et al. 2021; J. Matthee et al. 2023; G. Prieto-Lyon et al. 2023; P. Rinaldi et al. 2023; K. I. Caputi et al. 2024). We highlight that an increase in flux is also observed in the NIRCam longest

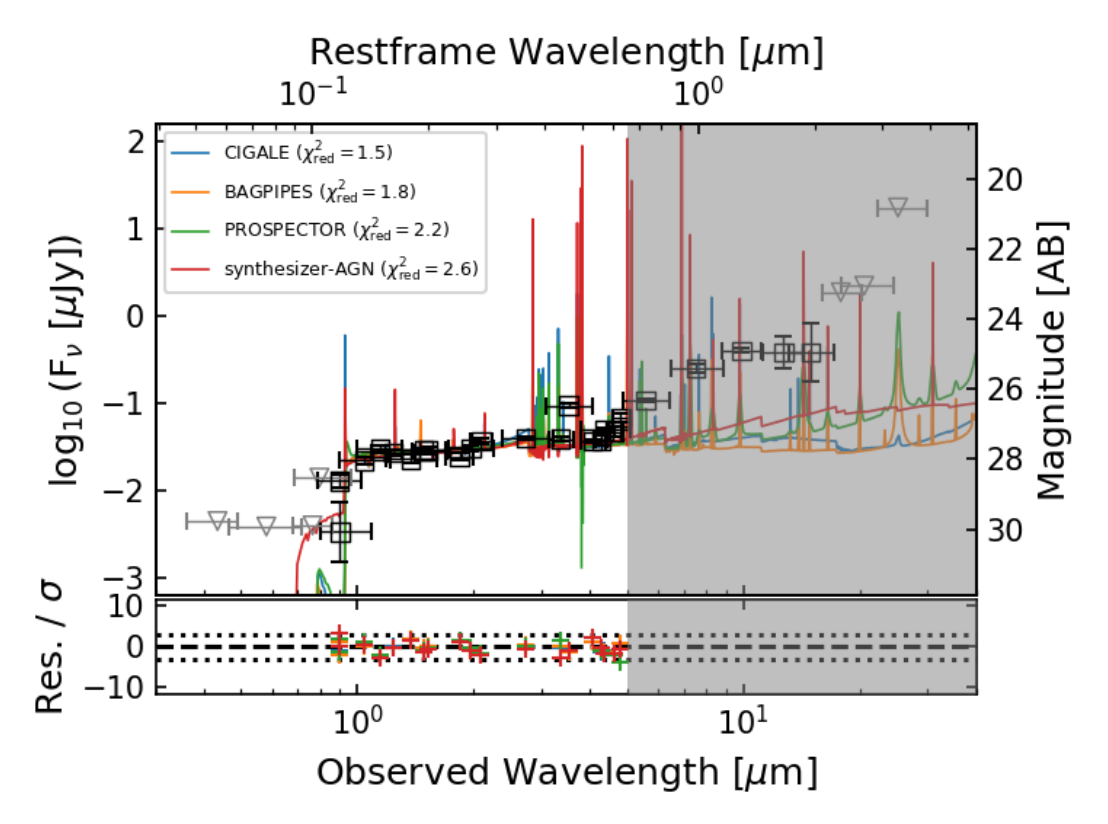


Figure 6. Virgil's photometry (black open squares and gray triangles for the upper limits) and best-fit models obtained with the SED-fitting codes CIGALE (blue) and BAGPIPES (orange) when limiting the analysis to the HST + JWST/NIRCam coverage, i.e., up to about 5 μ m (rest frame 0.65 μ m). The gray-shaded area is indicative of rest-frame wavelengths above 0.65 μ m. The SED fittings performed in this case do not include any AGN contribution. The bottom panel shows the ratio between the residuals (i.e., the synthetic minus the observed photometry) and the photometric error σ for all the available bands. The dotted lines are indicative of residuals equal to $\pm 3\sigma$.

wavelength filter, e.g., F460M – F480M = 0.39 \pm 0.19. At Virgil's redshift and without the information coming from the MIRI imaging, this flux excess could be easily ascribed to the H α emission line entering the F480M filter. In fact, medium-band filters are known for their heightened sensitivity to strong emission lines (e.g., C. Papovich et al. 2023; P. Rinaldi et al. 2023; K. I. Caputi et al. 2024).

Hence, by limiting the analysis of Virgil at rest-frame wavelengths $\leq 0.65 \, \mu \text{m}$, the observed SED of Virgil is well represented by a typical LAEs' SED with strong optical emission lines (e.g., M. Ouchi et al. 2020). This is also confirmed by our runs with SED-fitting codes only considering the available photometry below the MIRI/F560W imaging. In this case, all codes model Virgil as a young ($\leq 100 \, \text{Myr}$) star-forming (SFR = $1-2 \, M_{\odot} \, \text{yr}^{-1}$) low-mass galaxy ($M_{\star} \simeq 10^{8.0-8.5} \, M_{\odot}$) with low dust content ($A_V \leq 0.8 \, \text{mag}$), see Figure 6.

4.2. Virgil's Full SED

The distinctive feature of Virgil lies in its pronounced increase in brightness beyond the 0.6 μm rest frame (4.8 μm observed frame), leading to a notable upturn in its SED at NIR wavelengths. By fitting a power law ($f_{\lambda} \propto \lambda^{\alpha_{\rm NIR}}$) to the observed fluxes in the wavelength range of 4–10 μm (observed), we find a spectral index of $\alpha_{\rm NIR}=2.8\pm0.1$. While the increase in the reddest NIRCam medium-band filters F460M and F480M could be potentially caused by the presence of a strong H α +[N II] $\lambda\lambda$ 6548, 6584 line complex (e.g., C. Papovich et al. 2023), the steep rising MIRI SED from 0.7 μm (F560W) up to 1.3 μm (F1000W) rest frame cannot be solely explained by strong

emission lines. In fact, although at z = 6.6312 the Paschen- β (Pa\beta) emission line enters the F1000W band, atomic physics predicts that the Pa β intensity is about 1/20 of the H α line (assuming case B recombination, e.g., D. E. Osterbrock & G. J. Ferland 2006). Besides, F1000W is a very wide band, with an effective width of about 17000 Å. Hence, for a galaxy at Virgil's redshift, already an excess of 0.1 mag in F1000W would imply a rest-frame equivalent width for the emission line of about 200 Å, i.e., roughly one-third of what we estimate for the H β + [O III] complex. Based on our previous best SEDfitting models (see Section 4.1 and Figure 6), we would expect an excess of more than 2.0 mag with respect to the models' continuum in F1000W, thus implying an unrealistically strong $Pa\beta$ line. A similar reasoning can be applied to Virgil's detection (S/N \approx 5) in F770W (effective width of about 18300 Å), with a flux \approx 2.5 times higher than what we detect in F560W (F560W – F770W = 1.01 ± 0.23).

Having excluded that the red upturn is driven by strong emission lines, we fit Virgil's observed photometry (including the ALMA upper limits at 1.2 and 3 mm) in a twofold way: assuming that its SED is uniquely due to the contribution of stellar populations and the ISM, and adding the effects of an AGN. In fact, Virgil's steep rise in SED at the rest-frame NIR domain of galaxy spectra could be a sign of an AGN dusty torus (e.g., R. C. Hickox & D. M. Alexander 2018).

4.2.1. Only Stellar Population Models

When implementing only stellar populations (see Table 2), in general, we struggle to reproduce Virgil's overall SED and

Table 2
Stellar SED Properties of Virgil—Only Stars

Code	$\chi^2_{\rm red}$	$\frac{\log_{10}(M_\star)}{\log_{10}([M_\odot])}$	$A_{V,\mathrm{main}}$ (mag)	Age _{main} (Myr)	$A_{V, m young} \ m (mag)$	Age _{young} (Myr)	Age _{mass-weighted} (Myr)	$\frac{\text{SFR}_{100 \text{ Myr}}}{(M_{\odot} \text{ yr}^{-1})}$
SYNTHESIZER-AGN	6.5	9.71 ± 0.10	4.00 ± 0.1	26 ± 4	0.50 ± 0.01	6 ± 1	32+9	
CIGALE	19.4	8.95 ± 0.08	0.81 ± 0.04	304 ± 223	•••	3 ± 1	275 ± 104	2.60 ± 0.87
BAGPIPES	20.6	$8.74^{+0.38}_{-0.12}$	$0.73^{+0.05}_{-0.09}$	720^{+70}_{-230}		20^{+2}_{-1}	220^{+370}_{-130}	$3.42^{+0.67}_{-1.35}$
PROSPECTOR	25.1	$9.01^{+0.03}_{-0.16}$	$0.12^{+0.02}_{-0.01}$	•••			367^{+51}_{-33}	$2.53^{+0.51}_{-1.90}$

Note. In the above table, we report the main physical properties of Virgil as derived from the different SED-fitting codes adopted in our study: SYNTHESIZER-AGN, CIGALE, BAGPIPES, and PROSPECTOR. In this table, we present the results derived when considering only the contribution of stellar populations to the overall Virgil's SED. Specifically, we report the logarithm of the stellar mass $\log_{10}(M_{\star})$, the extinction of the main stellar component $A_{V,\text{main}}$ and its age Age_{main} , the extinction of the young stellar component $A_{V,\text{young}}$ and its age Age_{young} , the mass-weighted age of the overall galaxy $Age_{\text{mass-weighted}}$ and its average SFR over the last 100 Myr SFR $_{100 \text{ Myr}}$. Cells with \cdots denote parameters where the codes do not provide an estimate.

behavior at the MIRI wavelengths. The only code that can reproduce Virgil's photometry and its red MIRI slope with solely stellar populations is SYNTHESIZER-AGN ($\chi^2_{\rm red} = 6.9$) thanks to a combination of two subsolar ($Z \simeq 0.4Z_{\odot}$) young populations (6 and 26 Myr old) with very different extinctions $(A_V = 0.5, 4.0 \text{ mag})$ and combined with a very strong contribution from the nebular continuum, see Figure 7 (top panel). Due to the presence of the heavily attenuated second stellar component, the total mass of Virgil retrieved by SYNTHESIZER-AGN is $M_{\star}=10^{9.7\pm0.1}M_{\odot}$. From the best-fit model, we also derive a total SFR(UV) $\approx 69 M_{\odot} \text{ yr}^{-1}$ (corrected for dust extinction). This solution would suggest a scenario for Virgil as a dusty starburst galaxy. In this case, the blue and red components of the SED would arise from different parts of the galaxy. The relatively small angular size of Virgil, together with the coarser MIRI resolution and the presence of the lower redshift contaminant (Section 3.3) prevent us, however, from further investigating this scenario based on the currently available data. Nonetheless, we highlight that in this scenario, classical templates of dust emission (e.g., R. Chary & D. Elbaz 2001) with dust temperatures of $T_{\text{dust}} = 20\text{--}30 \text{ K}$ dominating the dust mass would not comply with the ALMA upper limits for a total absorbed energy of $L_{\rm dust} \approx 10^{11.5} L_{\odot}$. Only assuming models with higher dust temperatures (≈60–70 K; e.g., R. Siebenmorgen & E. Krügel 2007; C. Schreiber et al. 2018; L. Sommovigo et al. 2020, 2022) would allow us to meet the upper limits at wavelengths >1 mm, see Figure 8.

The flexibility of SYNTHESIZER-AGN in finding such a best-fit result is hardly retrievable with the other SED-fitting codes at our disposal and which struggle to return good best-fit models ($\chi^2_{\rm red} \gtrsim 20$), failing in reproducing the photometry at the MIRI wavelengths. In this context, CIGALE, BAGPIPES, and PROSPECTOR find very similar best-fit parameters, i.e., $M_{\star} \simeq 10^9 \, M_{\odot}$, SFR $\simeq 3 \, M_{\odot} \, {\rm yr}^{-1}$, $A_V \leqslant 0.8$ mag, and a mass-weighted age of about 300 Myr.

Interestingly, if we try to fit a graybody emission $(f_{\lambda} \propto \lambda^{-\beta-3}/(e^{\frac{hc}{M_{\rm B}T}}-1))$, e.g., K. I. Caputi 2013) to the residuals of the MIRI data points, i.e., after subtracting the best-fit models derived by these three different codes from the observed photometry, we find a graybody temperature of $T=1762^{+177}_{-143}$ K (if we assume $\beta=1.5$). Such a high value of the graybody temperature is comparable to the typical values for the sublimation of dust $(T_{\rm sub} \approx 1500-2000$ K, depending on the dust composition, e.g., M. J. Temple et al. 2021) and is hardly reconcilable with heating due to normal stellar activity

(even in the case of very compact, intense starbursting regions; e.g., M. E. De Rossi et al. 2018; L. Sommovigo et al. 2020).

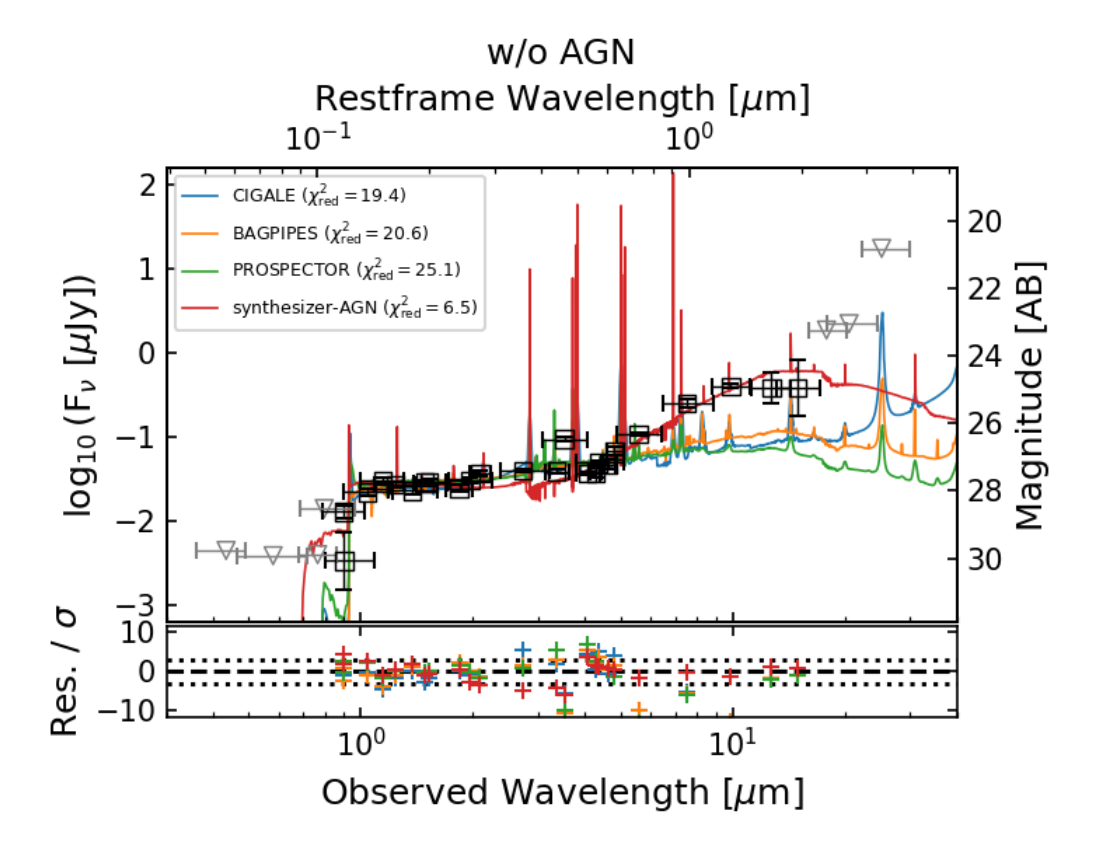
4.2.2. Stellar Population and AGN Models

To improve the best-fit models, we consider adding an AGN component to the fits. As a first step, we verify if Virgil is an already known AGN in the literature. To this purpose, we look for possible counterparts of Virgil in the available AGN catalogs in HUDF based on both observations by Chandra (e.g., B. Luo et al. 2017; I. N. Evans et al. 2020) and XMM-Newton (P. Ranalli et al. 2013), but find no X-ray counterpart.

To assess if Virgil is a weak X-ray emitter and its absence in the X-ray catalogs is not merely due to the depth of the available Chandra and XMM-Newton observations, we estimate an upper limit over its rest-frame X-ray to optical-UV ratio $\alpha_{\rm ox} = -\log_{10}[L(2~{\rm keV})/L(2500~{\rm Å})]/2.605$ (e.g., H. Tananbaum et al. 1979; E. Lusso et al. 2010). While we derive Virgil's luminosity at 2500Å $L(2500~{\rm Å})$ directly from the available JWST/NIRCam photometry ($L(2500~{\rm Å}) \approx 1.98 \times 10^{28}~{\rm erg~s^{-1}~Hz^{-1}}$), we infer the luminosity at 2 keV $L(2~{\rm keV})$ by considering 3 times the limiting flux of the deepest X-ray observations (i.e., Chandra) in the soft band (0.5–2 keV) for the HUDF (B. Luo et al. 2017) and obtain $L_{2\rm keV} \approx 3.48 \times 10^{25}~{\rm erg~s^{-1}~Hz^{-1}}$. These estimates imply $\alpha_{\rm ox} \gtrsim 1.25$, a range of values for which the rest-frame UV emission of the galaxy dominates over the X-rays, thus confirming the intrinsic weak X-ray nature of Virgil.

In addition to the X-ray-based catalogs of AGN, we searched for possible counterparts for Virgil in the catalog by J. Lyu et al. (2022), which extended AGN detection in the HUDF by analyzing galaxies' rest-frame optical-to-mid-infrared emission. We also examined the recently released AGN catalog by J. Lyu et al. (2024), based solely on MIRI imaging from the SMILES program. In both cases, no previously identified AGN is found at the coordinates of our target.

As a result of our SED-fitting runs on the whole available photometry (ALMA upper limits included), we find that all codes prefer the SED solution implementing an AGN to the case of only stellar populations, delivering better quality fits (i.e., lower $\chi^2_{\rm red}$), see Figure 7 (bottom panel) and Table 3. In this case, the best fits are provided by SYNTHESIZER-AGN ($\chi^2_{\rm red}=5.4$) and CIGALE ($\chi^2_{\rm red}=6.9$). For SYNTHESIZER-AGN, the best fit indicates a total stellar mass $M_\star\simeq 10^{8.2}\,M_\odot$ with two young stellar populations: a 1 Myr old stellar population with a metallicity $Z=0.2Z_\odot$ and $A_V=0.5$, and a 25 Myr old stellar population of solar metallicity and $A_V=0.9$. The smaller stellar mass of this run with respect to the



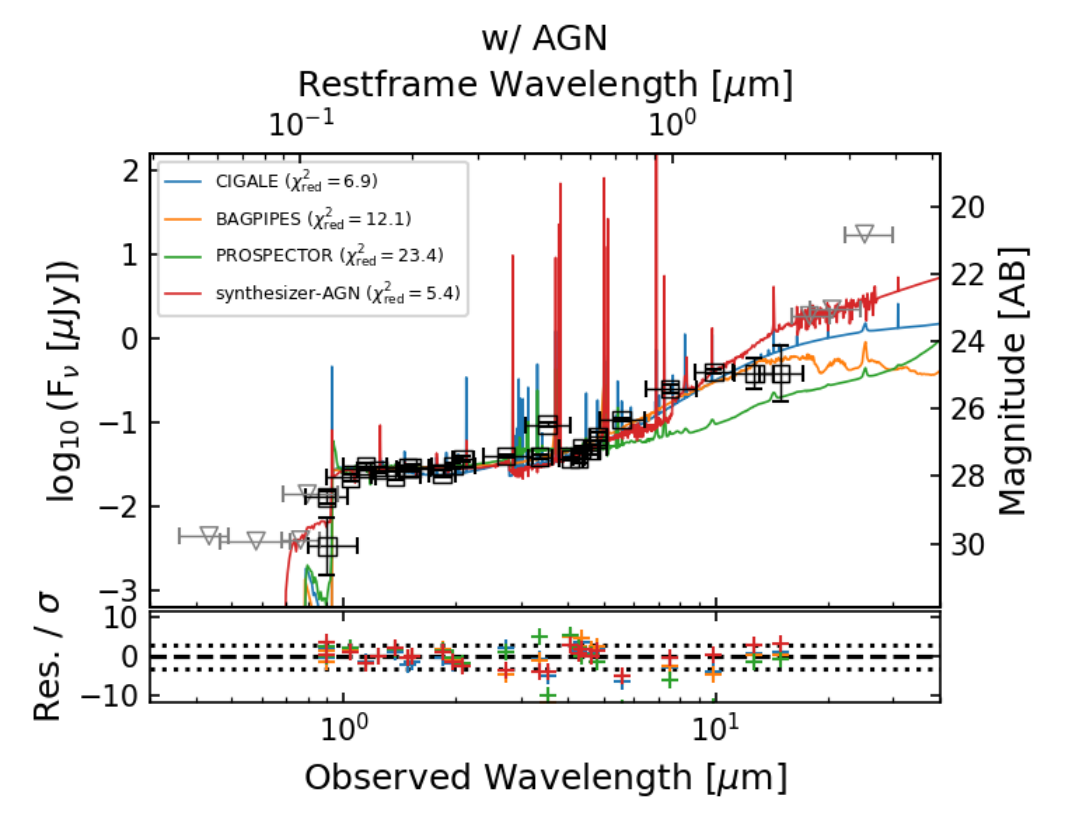


Figure 7. Virgil's photometry (black open squares and gray triangles for the upper limits) and best-fit models obtained with the SED-fitting codes CIGALE (blue), BAGPIPES (orange), PROSPECTOR (green), and SYNTHESYZER-AGN (red) in the case of excluding (upper panel) and assuming (lower panel) an AGN component. The bottom panel shows the ratio between the residuals and the photometric error σ for all the available bands. The dotted lines are indicative of residuals equal to $\pm 3\sigma$. For the sake of clarity, we limit the above panels to wavelengths $<40\mu m$ even if the ALMA upper limits were taken into account during the fitting procedure.

Table 3					
Stellar SED	Properties of Virgil-Stars and AGN				

Code	$\chi^2_{\rm red}$	$\log_{10}(M_{\star}) \\ \log_{10}([M_{\odot}])$	$A_{V,\mathrm{main}}$ (mag)	Age _{main} (Myr)	$A_{V, ext{young}}$ (mag)	Age _{young} (Myr)	Age _{mass-weighted} (Myr)	$\frac{\text{SFR}_{100 \text{ Myr}}}{(M_{\odot} \text{ yr}^{-1})}$
SYNTHESIZER-AGN	5.4	8.19 ± 0.07	0.90 ± 0.10	2.5 ± 0.5	0.46 ± 0.03	1 ± 0.5	$0.8^{+0.8}_{-0.2}$	
CIGALE	6.9	8.50 ± 0.02	0.83 ± 0.04	662 ± 230	•••	1.5 ± 0.5	309 ± 121	0.88 ± 0.04
BAGPIPES	12.1	$10.25^{+0.04}_{-0.05}$	$3.57^{+0.18}_{-0.17}$	790^{+20}_{-30}		260^{+20}_{-60}	640^{+20}_{-110}	
PROSPECTOR	23.4	$8.77^{+0.06}_{-0.11}$	$0.11^{+0.01}_{-0.02}$				284^{+31}_{-32}	$2.50^{+0.53}_{-1.75}$

Note. As in Table 2, we report the main physical properties of Virgil as derived from the different SED-fitting codes adopted in our study. In this table, we present the results derived when adding to the contribution of stellar populations also an AGN component.

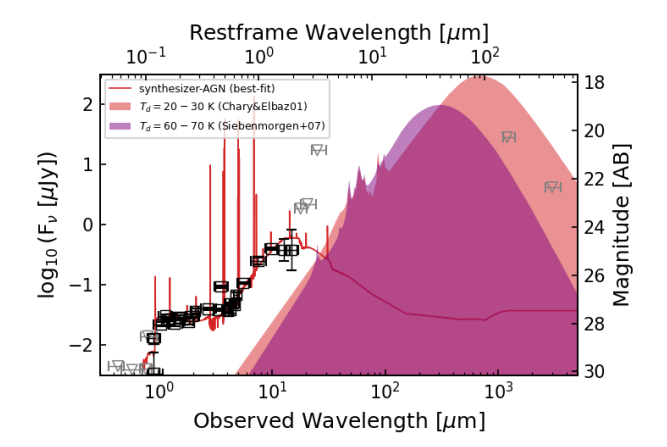


Figure 8. Decomposition of the dust component from Virgil's photometry (black open squares and gray triangles for the upper limits) for the best-fit model obtained with the SED-fitting code SYNTHESIZER-AGN (red). The redshaded area is indicative of the model of dust emission with temperatures of 20–30 K (R. Chary & D. Elbaz 2001) for a $L_{\rm dust} \approx 10^{11.5}\,L_{\odot}$ (as predicted from SYNTHESIZER-AGN). The purple-shaded area represents a model with higher dust temperature (60–70 K, R. Siebenmorgen & E. Krügel 2007). In the case of two populations and strong attenuation, only models with higher $T_{\rm dust}$ can comply with the ALMA upper limits.

no-AGN case is due to the dominant contribution at the NIR wavelengths of the AGN component. In the case of CIGALE, Virgil's best fit has a stellar mass of $M_{\star} \simeq 10^{8.5 \pm 0.2} M_{\odot}$ and is reproduced with a young (3 Myr) and an older (300 Myr) stellar population with solar metallicities and $A_V = 0.8$. Also for CIGALE, the AGN dominates at the longest MIRI wavelengths, see Figure 9.

We further investigate the properties of the eventual AGN hosted in Virgil by estimating its bolometric luminosity $L_{\rm AGN,bol}$ and supermassive black hole mass $M_{\rm BH}$. Following S. Kaspi et al. (2000), we derive $L_{\rm AGN,bol}$ from the monochromatic luminosity at 5100 Å (corrected for dust extinction) $L(5100~{\rm \AA})$ as $L_{\rm AGN,bol}\approx 9\cdot\lambda\cdot L(5100~{\rm \AA})$. In the case of Virgil, the estimated luminosity at 5100 Å is $L(5100~{\rm \AA})\approx 2.9\times 10^{39}~{\rm erg~s^{-1}~\AA^{-1}}$. However, according to our best fit with CIGALE, at 5100 Å (rest frame) the AGN contributes only to 40% of the observed emission. Besides, the AGN's dust attenuation is $A(5100~{\rm \AA})\approx 3.3~{\rm mag}$. Therefore, correcting for AGN contribution and dust obscuration, we estimate $L_{\rm AGN}(5100~{\rm \AA})\approx 2.4\times 10^{40}~{\rm erg~s^{-1}~\AA^{-1}}$, which converts into an $L_{\rm AGN,bol}\approx 1.1\times 10^{45}~{\rm erg~s^{-1}~\AA^{-1}}$, which converts into an $L_{\rm AGN,bol}\approx 1.1\times 10^{45}~{\rm erg~s^{-1}}$. We recover similar values also when considering the best-fit results from SYNTHESIZER-AGN: $L_{\rm AGN}(5100~{\rm \AA})\approx 1.9\times 10^{40}~{\rm erg~s^{-1}~\AA^{-1}}$ and $L_{\rm AGN,bol}\approx 8.9\times 10^{44}~{\rm erg~s^{-1}}$. By comparing the soderived AGN bolometric luminosity to the Eddington

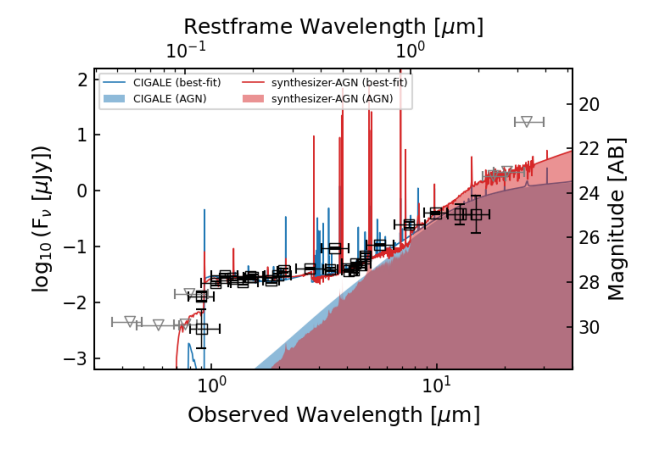


Figure 9. Decomposition of the AGN component from Virgil's photometry (black open squares and gray triangles for the upper limits) for the best-fit models obtained with the SED-fitting codes CIGALE (blue) and SYNTHESIZER-AGN (red).

luminosity $L_{\rm Edd}$ (A. S. Eddington 1926), we can infer $M_{\rm BH}$ via the relation $M_{\rm BH}=7.9\times10^{-39}\times(L_{\rm AGN,bol}/\lambda_{\rm Edd})$, where $\lambda_{\rm Edd}$ is the Eddington ratio. Considering typical values for the Eddington ratio $\lambda_{\rm Edd}=0.1$ –1, the range of values we obtain for the mass of the supermassive black hole of our target varies from $M_{\rm BH}\approx(7-9)\times10^6\,M_\odot$ ($\lambda_{\rm Edd}=1$) to $M_{\rm BH}\approx(7-9)\times10^7\,M_\odot$ ($\lambda_{\rm Edd}=0.1$). These estimates are in good agreement with the values of bolometric luminosity of AGNs at z>4 recently studied with JWST (V. Kokorev et al. 2023; L. J. Furtak et al. 2024; J. E. Greene et al. 2024; J. Matthee et al. 2024).

4.2.3. Virgil, an LRD?

The flat rest-frame UV and the red NIR colors of Virgil revealed by our multiwavelength data set (HST, JWST NIRCam, and MIRI) are similar to the "v-shaped" SED (in the λ - f_{λ} plane) of the recently discovered population of LRDs (e.g., L. J. Furtak et al. 2023; I. Labbe et al. 2023; H. B. Akins et al. 2024; V. Kokorev et al. 2024; J. Matthee et al. 2024; P. G. Pérez-González et al. 2024b). Despite the rapid emergence of LRDs in the literature over the past 2 yr, their nature and unusual SEDs remain largely unexplained. Proposed explanations suggest a complex interplay between AGN activity, stellar populations, and dust (K. Inayoshi & K. Ichikawa 2024; I. Labbe et al. 2023; Y. Li et al. 2024). While this debate continues, the detection of broad Balmer lines (e.g., $H\alpha$, $H\beta$) in some LRDs has been interpreted as strong evidence for AGN activity, implying accretion onto supermassive black holes (S. Fujimoto et al. 2024; L. J. Furtak

et al. 2024; V. Kokorev et al. 2023; J. E. Greene et al. 2024; M. Killi et al. 2024; J. Matthee et al. 2024).

Following V. Kokorev et al. (2024), Virgil's photometry complies with most of the color criteria used to characterize LRDs at z > 6. In particular, for Virgil we find:

1. F150W – F200W = $0.05 \pm 0.10(< 0.8)$; 2. F277W – F356W = $0.92 \pm 0.07(> 0.6)$; 3. F277W – F444W = $0.22 \pm 0.07(> 0.7)$; 4. F115W – F200W = $-0.01 \pm 0.10(> -0.5)$;

where the values in parentheses indicate the selection criteria from V. Kokorev et al. (2024), designed to identify "v-shaped" SEDs while minimizing contamination from brown dwarfs (particularly the F115W – F200W condition). The only discrepancy is Virgil's F277W – F444W color, which appears bluer than expected for LRDs. However, at the specific redshift of our target (z = 6.63124), this could be explained by the positioning of the filters relative to strong nebular lines. The F444W filter probes wavelengths redward of [O III] and blueward of H α . At the wavelengths of these strong optical emission lines, the transmission drops below 5%, making the F444W quite robustly probe the optical continuum without significant contamination from such strong transitions. This may result in a bluer color. Indeed, replacing F444W with the adjacent MIRI filter F560W reveals a significantly redder color: $F277W - F560W = 1.10 \pm 0.06$.

At rest-frame UV wavelengths, Virgil meets the brown dwarf rejection criteria from V. Kokorev et al. (2024). However, it does not strictly comply with the F150W – F200W color threshold proposed by D. Langeroodi & J. Hjorth (2023a), who suggest that objects with F150W – F200W < 0.25 are typically brown dwarfs. Nonetheless, Virgil's F277W – F444W color places it outside the region occupied by brown dwarfs in the F277W – F444W versus F150W – F200W diagram (see Figure 13 of D. Langeroodi & J. Hjorth 2023a). Additionally, its extended morphology further rules out the brown dwarf hypothesis.

The estimate of the compactness parameter (c = f(r = 0.2)/f(r = 0.1)) with fluxes properly corrected for aperture) derived from the F444W image after removing contamination from the nearby LAE (see Section 3.3) yields $c_{\rm F444W} \approx 1.5$, thus satisfying the LRD compactness criterion $c_{\rm F444W} < 1.7$.

Despite not fully meeting the LRDs' F277W – F444W color, Virgil complies with all the other LRD criteria adopted in the recent literature. This shows that our target is likely to be the first LRD with a detectable host galaxy from rest-frame UV-to-optical wavelengths (see Section 3.4). In this regard, M. Killi et al. (2024) already reported an LRD at $z\approx 4.5$ with a slightly more extended rest-frame UV morphology than previously assumed for this class of sources. Furthermore, following our discovery of Virgil, additional LRDs have been identified with extended and more complex UV morphologies than simple PSF-like profiles (P. Rinaldi et al. 2024). Virgil, however, would be the first LRD with a clear detection of its host galaxy, having a resolved morphology down to its rest-frame optical wavelengths. Overall, these findings suggest a broader diversity among LRDs than initially anticipated.

To further corroborate Virgil's resemblance to LRDs, we compare its photometry to empirical SEDs derived from stacked LRDs, including the average SED of 20 MIRI-detected LRDs in the HUDF (P. G. Pérez-González et al. 2024a) and the "maximal" SED from stacking 500 LRDs in

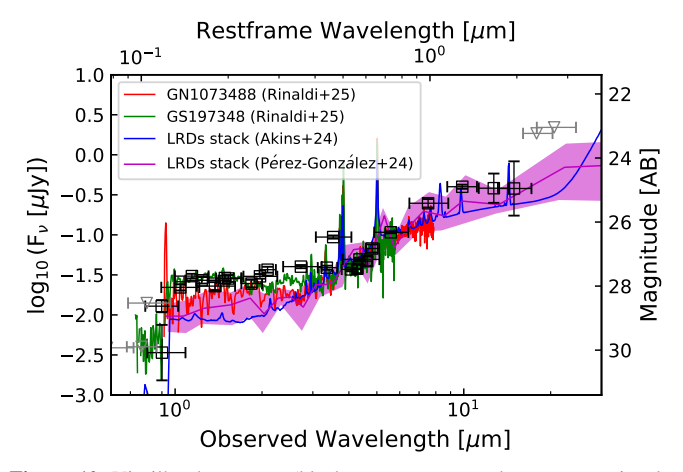


Figure 10. Virgil's photometry (black open squares and gray open triangles for the 3σ upper limits) and the average observed SED of MIRI-detected LRDs (in magenta) found in the HUDF and reported by P. G. Pérez-González et al. (2024a). In blue, the "maximal" SED of 500 LRDs detected in COSMOS-Webb (H. B. Akins et al. 2024), while in red and green the NIRCam/MSA spectra of two LRDs in HUDF (P. Rinaldi et al. 2024).

the COSMOS-Webb field (H. B. Akins et al. 2024) (see Figure 10). After redshifting these empirical SEDs to z=6.63124 and normalizing their fluxes to match Virgil's photometry, we find a strong agreement at rest-frame optical/NIR wavelengths. However, at shorter wavelengths (rest-frame UV), the empirical SEDs lie below Virgil's observed photometry. This could be the wavelength regime where Virgil's underlying stellar emission could contribute more to its overall emission, suggesting that its stronger UV emission could be mainly attributed to young stellar populations, as also found from our SED fitting (see Section 3.7).

We also compare Virgil's photometry with the NIRCam/MSA spectra of two LRDs detected in the HUDF (P. Rinaldi et al. 2024). The best match is with GS197348 (green spectrum; A. J. Bunker et al. 2023; P. Rinaldi et al. 2024), which closely reproduces Virgil's SED, even at rest-frame UV wavelengths. This further highlights that while LRDs share similar optical/NIR properties, their UV emission can vary significantly from object to object.

Interestingly, Virgil's nondetection in X-rays (Section 4.2) is consistent with recent findings for LRDs (T. T. Ananna et al. 2024; M. Yue et al. 2024). Similarly, the nondetection at FIR wavelengths (ALMA upper limits) is in agreement with general LRD findings (I. Labbe et al. 2023; P. G. Pérez-González et al. 2024a; C. C. Williams et al. 2024).

Once again, we emphasize the critical role of MIRI data in this classification. Without MIRI imaging, identifying Virgil as a "v-shaped" object would have been impossible. In addition, we highlight that existing LRD selection criteria (based solely on NIRCam photometry) extend only to rest-frame optical wavelengths near $H\alpha$ at z>6. This means that they miss the rising NIR red continuum of LRDs and are susceptible to contamination from strong line emitters (e.g., K. N. Hainline et al. 2025). Incorporating MIRI data is therefore essential for robustly identifying this population at z>6.

4.3. The Impact of Long-wavelength MIRI Filters

A final remark comes from the information that we can obtain thanks to the presence of the longest MIRI wavelengths (i.e., F1280W, F1500W). Despite the shallower depth of the

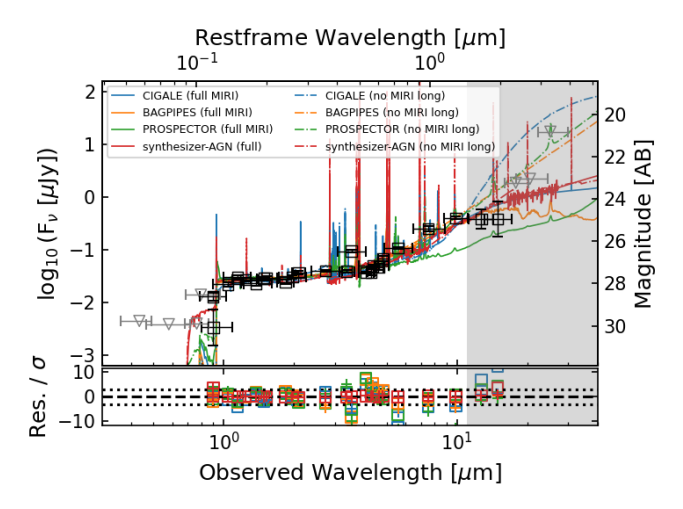


Figure 11. Virgil's photometry (as in the previous panels) and best-fit models obtained with the SED-fitting codes CIGALE (blue), BAGPIPES (orange), PROSPECTOR (green), and SYNTHESYZER-AGN (red) in the case of excluding (dashed-dotted lines) and assuming (solid lines) the photometric MIRI information at >10 μm (gray-shaded area). Similarly, the bottom panel shows the ratio between the residuals and the photometric error for all the available bands when excluding (plus) and assuming (open squares) the MIRI long-wavelength filters. The dotted lines are indicative of residuals equal to $\pm 3\sigma$.

available imaging above 10 μ m, we find that the steep rise observed up to F1000W could tend to flatten at longer wavelengths (above the rest frame 1.6 μ m). Interestingly, such flattening of the SED was also reported in the average trend of the MIRI-detected LRDs by C. C. Williams et al. (2024) and P. G. Pérez-González et al. (2024a). Also, B. Wang et al. (2025) revealed an unexpected flattening at rest-frame wavelengths of 0.7–5 μ m in their spectrophotometric study of an LRD at $z\approx 3.1$. The origin of this flattening is still debated, but in the AGN scenario, one possible explanation (B. Wang et al. 2025) could be a lack of torus emission as in the case of hot-dust-deficient AGNs (e.g., L. Jiang et al. 2010; J. Lyu et al. 2017; S. Son et al. 2023).

Due to the higher redshift of our target, we have a hint of flattening only from the F1280W and F1500W filters, probing the rest-frame 1.6–2 μm wavelength range. We retrieve an estimate of the flux in F1280W (S/N \approx 2.4) and F1500W (S/N \approx 1.3), which imply colors of F1000W – F1280W = 0.1 \pm 0.2 and F1000W – F1500W = 0.1 \pm 0.3. The shallower depth of the available MIRI filters $\lambda >$ 18 μm prevents us from robustly confirming the flattening on a longer wavelength range. Deeper F1800W and F2100W imaging would be necessary to extend this finding up to 3 μm (rest frame).

We underline how, if the flattening trend is confirmed, without any information at these wavelengths, the SED codes would tend to prefer models that keep on rising, thus overpredicting the flux at the longest wavelengths and overestimating the importance of the AGN dust torus, see Figure 11. This further underlines the importance of conducting deep MIRI imaging above the $10~\mu m$, even if challenged by the lower sensitivity of the MIRI instrument at such wavelengths.

5. Summary and Conclusions

In this paper, we have presented the analysis of Virgil, a MERO detected with the F1000W filter as part of the MIDIS

observations of the HUDF. Virgil is an LAE at $z = 6.63124 \pm 0.00188$ (VLT/MUSE; R. Bacon et al. 2023) showing a red F444W – F1000W = 2.33 ± 0.06 color.

The extracted photometry of Virgil shows a blue UV continuum ($\beta_{\rm UV} = -2.1 \pm 0.3$), the presence of strong emission lines (flux excess of the F356W band corresponding to the H β + [O III] complex) and a steep rising SED from 0.7 to 1.3 μ m (rest frame). SED-fitting models considering only stellar populations struggle to explain Virgil's behavior at MIRI wavelengths. The best-fit model suggests that Virgil's SED originates from two components: an extremely young (6 Myr) and unobscured stellar population dominating the blue wavelengths, and another young (26 Myr) stellar population strongly affected by extinction ($A_V = 4$ mag), which is responsible for most of the light at red wavelengths. In agreement with recent papers on LRDs (G. Barro et al. 2024; P. G. Pérez-González et al. 2024a; C. C. Williams et al. 2024), in this scenario, the bulk of the dust re-emitting the absorbed light at rest-frame UV and optical wavelengths should be hotter than 60–70 K to comply with the ALMA upper limits. This temperature is significantly higher than the one typically adopted for SED fitting (i.e., 20-30 K; e.g., R. Chary & D. Elbaz 2001). In this case, Virgil could be similar to a dusty starburst. The small angular size of Virgil, together with the coarser MIRI resolution, hamper us from deriving whether the two populations are located in different parts of the galaxy. All the other codes fail to reproduce the steep and rising MIRI photometry.

Such a red rising part of Virgil's SED could hint at the presence of a (dust-obscured) AGN. Despite extensive searches, no AGN counterparts have been found in existing multiwavelength catalogs (P. Ranalli et al. 2013; B. Luo et al. 2017; I. N. Evans et al. 2020; J. Lyu et al. 2022, 2024). However, when implementing an AGN contribution to the SED, all the SED-fitting codes adopted deliver significantly improved best-fit models. Assuming the presence of an AGN, we estimate a bolometric luminosity of $L_{\rm bol,AGN} \approx (8.9-11) \times$ $10^{44} \, \mathrm{erg \, s^{-1}}$ and an $M_{\mathrm{BH}} = (7-9) \times 10^6 \, M_{\odot}$ (if $\lambda_{\mathrm{Edd}} = 1$). These estimates agree with those reported in the recent literature targeting reddened AGNs at z > 4 (e.g., V. Kokorev et al. 2023; J. Scholtz et al. 2025; L. J. Furtak et al. 2024; J. Matthee et al. 2024; P. Rinaldi et al. 2024). Nonetheless, with the currently available data is difficult to fully rule out one of the proposed scenarios. We cannot even exclude that the two conditions (dusty starburst and AGN) could be true at the same time, i.e., not too differently from what was recently reported for the GN20 galaxy at z = 4.05 (e.g., L. Colina et al.

2023; H. Übler et al. 2023; A. Bik et al. 2024; D. Crespo et al. 2024).

Virgil's flat rest-frame UV and red NIR colors, and in general, the shape of its SED, suggest that our target belongs to the recently discovered population of LRDs (e.g., I. Labbe et al. 2023; V. Kokorev et al. 2024; P. G. Pérez-González et al. 2024a). This is further confirmed by the comparison of Virgil's SED with the recently reported empirical SED (H. B. Akins et al. 2024; P. G. Pérez-González et al. 2024a) and the actual spectra of other LRDs (P. Rinaldi et al. 2024). However, the extended morphology of Virgil at UV-to-optical wavelengths makes it the first LRD for which we can clearly detect the host galaxy.

Despite the richness of the photometric data set available, deeper MIRI long-wavelength observations in combination with a rest-frame optical and NIR spectroscopic follow-up (as demonstrated in recent literature, e.g., Y. Li et al. 2024; S. Tacchella et al. 2025; B. Wang et al. 2025) appear to be fundamental to properly assess the nature of Virgil.

All in all, our findings show the power of MIRI imaging in unveiling the complexity of this galaxy's nature. For our target, MIRI provides a fundamental piece of information that would be otherwise completely missed without imaging at such long wavelengths. This discovery opens up the question of how many objects like Virgil there are in the Universe. If a systematic search for similar objects in deep MIRI surveys reveals several Virgil-like objects and their AGN nature is confirmed, this discovery could potentially bring us to reassess (once more) the role of AGN in the reionization. In addition to a more general importance of MIRI in the characterization of galaxy properties, this study also advocates for the importance of conducting deep and extended MIRI surveys at $\lambda > 10 \,\mu \mathrm{m}$ wavelengths, a regime that results in being crucial in correctly determining the physical properties of galaxies and unveiling their hidden components. In fact, the absence of MIRI longwavelength photometry (even in the case of upper limits) biases us to overestimate the contribution of AGN in the SED of such objects.

Acknowledgments

The authors thank R. Cooper, G. Yang, V. Kokorev, D. Wen, C. Williams, and H. Übler for useful discussions and comments.

E.I. and K.I.C. acknowledge funding from the Netherlands Research School for Astronomy (NOVA). K.I.C. acknowledges funding from the Dutch Research Council (NWO) through the award of the Vici grant VI.C.212.036. A.A.-H. acknowledges support from grant PID2021-124665NB-I00 funded by MCIN/AEI/10.13039/ 501100011033 and by "ERDF A way of making Europe." P.G.P.-G. acknowledges support from grant PID2022-139567NB-I00 funded by the Spanish Ministerio de Ciencia e Innovación MCIN/AEI/ 10.13039/501100011033, FEDER Una manera de hacer Europa. J.A.-M., A.C.-G., and L.C. acknowledge support by grant PIB2021-127718NB-100 from the Spanish Ministry of Science and Innovation/State Agency of Research MCIN/ AEI/10.13039/501100011033 and by "ERDF A way of making Europe." L.C. thanks the support from the Cosmic Dawn Center received during visits to DAWN as an international associate. L.C. acknowledges support by grants PIB2021-127718NB-100 and PID2022-139567NB-I00 from the Spanish Ministry of Science and Innovation/State Agency

of Research MCIN/AEI/10.13039/501100011033 and by "ERDF A way of making Europe." T.R.G. acknowledges support from the Carlsberg Foundation (grant No. CF20-0534). S.G. acknowledges financial support from the Cosmic Dawn Center (DAWN), funded by the Danish National Research Foundation (DNRF) under grant No. 140. This work was supported by research grants (VIL16599, VIL54489) from VILLUM FONDEN. J.P.P. and T.V.T. acknowledge financial support from the UK Science and Technology Facilities Council and the UK Space Agency.

This work is based on observations made with the NASA/ ESA/CSA James Webb Space Telescope. The data were obtained from the MAST at the Space Telescope Science Institute, which is operated by the Association of Universities for Research in Astronomy, Inc., under NASA contract NAS 5-03127 for JWST. These observations are associated with programs GO #1963, GO #1895, and GTO #1283. The authors acknowledge the team led by co-PIs: C. Williams, M. Maseda, and S. Tacchella, and PI P. Oesch, for developing their respective observing programs with a zero-exclusiveaccess period. Also based on observations made with the NASA/ESA HST obtained from the Space Telescope Science Institute, which is operated by the Association of Universities for Research in Astronomy, Inc., under NASA contract NAS 5-26555. The work presented here is the effort of the entire MIRI team, and the enthusiasm within the MIRI partnership is a significant factor in its success. MIRI draws on the scientific and technical expertise of the following organizations: Ames Research Center, USA; Airbus Defence and Space, UK; CEA-Irfu, Saclay, France; Centre Spatial de Liège, Belgium; Consejo Superior de Investigaciones Científicas, Spain; Carl Zeiss Optronics, Germany; Chalmers University of Technology, Sweden; Danish Space Research Institute, Denmark; Dublin Institute for Advanced Studies, Ireland; European Space Agency, Netherlands; ETCA, Belgium; ETH Zurich, Switzerland; Goddard Space Flight Center, USA; Institute d'Astrophysique Spatiale, France; Instituto Nacional de Técnica Aeroespacial, Spain; Institute for Astronomy, Edinburgh, UK; Jet Propulsion Laboratory, USA; Laboratoire d'Astrophysique de Marseille (LAM), France; Leiden University, Netherlands; Lockheed Advanced Technology Center (USA); NOVA Opt-IR group at Dwingeloo, Netherlands; Northrop Grumman, USA; Max-Planck Institut für Astronomie (MPIA), Heidelberg, Germany; Laboratoire d'Etudes Spatiales et d'Instrumentation en Astrophysique (LESIA), France; Paul Scherrer Institut, Switzerland; Raytheon Vision Systems, USA; RUAG Aerospace, Switzerland; Rutherford Appleton Laboratory (RAL Space), UK; Space Telescope Science Institute, USA; Toegepast-Natuurwetenschappelijk Onderzoek (TNO-TPD), Netherlands; UK Astronomy Technology Centre, UK; University College London, UK; University of Amsterdam, Netherlands; University of Arizona, USA; University of Cardiff, UK; University of Cologne, Germany; University of Ghent; University of Groningen, Netherlands; University of Leicester, UK; University of Leuven, Belgium; University of Stockholm, Sweden; Utah State University, USA.

For the purpose of open access, the author has applied a Creative Commons Attribution (CC BY) licence to the Author Accepted Manuscript version arising from this submission.

Facilities: VLT:Yepun, HST, JWST, ALMA.

Software: ASTROPY (Astropy Collaboration et al. 2013, 2018, 2022), NUMPY (C. R. Harris et al. 2020), PANDAS (W. McKinney 2010; The pandas development team 2025), PHOTUTILS (L. Bradley et al. 2022), SCIPY (P. Virtanen et al. 2020), WEBBPSF (M. D. Perrin et al. 2014), SEXTRACTOR (E. Bertin & S. Arnouts 1996), LENSTRONOMY (S. Birrer & A. Amara 2018), SEP (K. Barbary et al. 2017), LEPHARE (O. Ilbert et al. 2006; S. Arnouts & O. Ilbert 2011), EAZY (G. B. Brammer et al. 2008), BAGPIPES (A. C. Carnall et al. 2018), CIGALE (D. Burgarella et al. 2005; S. Noll et al. 2009; M. Boquien et al. 2019), PROSPECTOR (B. D. Johnson et al. 2021), SYNTHESIZER-AGN (P. G. Pérez-González et al. 2003, 2008), ASTROPHOT (C. J. Stone et al. 2023), TOPCAT (M. Taylor 2011).

ORCID iDs

Edoardo Iani https://orcid.org/0000-0001-8386-3546
Pierluigi Rinaldi https://orcid.org/0000-0002-5104-8245
Karina I. Caputi https://orcid.org/0000-0001-8183-1460
Marianna Annunziatella https://orcid.org/0000-0002-8053-8040
Danial Langeroodi https://orcid.org/0000-0001-5710-8395
Jens Melinder https://orcid.org/0000-0003-0470-8754
Pablo G. Pérez-González https://orcid.org/0000-0003-4528-5639
Javier Álvarez-Márquez https://orcid.org/0000-0002-7093-1877
Leindert A. Boogaard https://orcid.org/0000-0002-3952-8588

Jens Hjorth https://orcid.org/0000-0002-4571-2306 Sarah Kendrew https://orcid.org/0000-0002-7612-0469 Alvaro Labiano https://orcid.org/0000-0002-0690-8824 John P. Pye https://orcid.org/0000-0002-0932-4330 Tuomo V. Tikkanen https://orcid.org/0009-0003-6128-2347

Fabian Walter https://orcid.org/0000-0003-4793-7880 Manuel Güdel https://orcid.org/0000-0001-9818-0588 Thomas Henning https://orcid.org/0000-0002-1493-300X Paul P. van der Werf https://orcid.org/0000-0001-5434-5942

References

```
Akins, H. B., Casey, C. M., Allen, N., et al. 2023, ApJ, 956, 61
Akins, H. B., Casey, C. M., Lambrides, E., et al. 2024, arXiv:2406.10341
Alberts, S., Lyu, J., Shivaei, I., et al. 2024, ApJ, 976, 224
Álvarez-Márquez, J., Colina, L., Crespo Gómez, A., et al. 2024, A&A, 686, A85
Ananna, T. T., Bogdán, Á., Kovács, O. E., Natarajan, P., & Hickox, R. C. 2024, ApJL, 969, L18
```

```
Arnouts, S., & Ilbert, O. 2011, LePHARE: Photometric Analysis for Redshift
   Estimate, Astrophysics Source Code Library, ascl:1108.009
Astropy Collaboration, Price-Whelan, A. M., Lim, P. L., et al. 2022, ApJ,
Astropy Collaboration, Price-Whelan, A. M., Sipőcz, B. M., et al. 2018, AJ,
   156, 123
Astropy Collaboration, Robitaille, T. P., Tollerud, E. J., et al. 2013, A&A,
Atek, H., Chemerynska, I., Wang, B., et al. 2023a, MNRAS, 524, 5486
Atek, H., Shuntov, M., Furtak, L. J., et al. 2023b, MNRAS, 519, 1201
Bacon, R., Accardo, M., Adjali, L., et al. 2010, Proc. SPIE, 7735, 773508
Bacon, R., Brinchmann, J., Conseil, S., et al. 2023, A&A, 670, A4
Bacon, R., Conseil, S., Mary, D., et al. 2017, A&A, 608, A1
Bagley, M. B., Pirzkal, N., Finkelstein, S. L., et al. 2024, ApJL, 965, L6
Barbary, K., Boone, K., Craig, M., Deil, C., & Rose, B., 2017 kbarbary/sep:
   v1.0.2, Zenodo, doi:10.5281/zenodo.896928
Barro, G., Perez-Gonzalez, P. G., Kocevski, D. D., et al. 2024, ApJ, 963, 128
Beckwith, S. V. W., Stiavelli, M., Koekemoer, A. M., et al. 2006, AJ,
   132, 1729
Bellovary, J. 2025, ApJL, 984, L55
Bertin, E., & Arnouts, S. 1996, A&AS, 117, 393
Bik, A., Álvarez-Márquez, J., Colina, L., et al. 2024, A&A, 686, A3
Birrer, S., & Amara, A. 2018, PDU, 22, 189
Boogaard, L. A., Gillman, S., Melinder, J., et al. 2024, ApJ, 969, 27
Boquien, M., Burgarella, D., Roehlly, Y., et al. 2019, A&A, 622, A103
Bouchet, P., Garcia-Marin, M., Lagage, P. O., et al. 2015, PASP, 127, 612
Boyett, K., Bunker, A. J., Curtis-Lake, E., et al. 2024, MNRAS, 535, 1796
Bradley, L., Sipocz, B., Robitaille, T., et al., 2022 astropy/photutils: v1.5.0,
   Zenodo, doi:10.5281/zenodo.6825092
Brammer, G. B., van Dokkum, P. G., & Coppi, P. 2008, ApJ, 686, 1503
Bruzual, G., & Charlot, S. 2003, MNRAS, 344, 1000
Bunker, A. J., Saxena, A., Cameron, A. J., et al. 2023, A&A, 677, A88
Burgarella, D., Buat, V., & Iglesias-Páramo, J. 2005, MNRAS, 360, 1413
Byler, N., Dalcanton, J. J., Conroy, C., & Johnson, B. D. 2017, ApJ,
   840, 44
Calzetti, D., Armus, L., Bohlin, R. C., et al. 2000, ApJ, 533, 682
Caputi, K. I. 2013, ApJ, 768, 103
Caputi, K. I., Dunlop, J. S., McLure, R. J., & Roche, N. D. 2004, MNRAS,
Caputi, K. I., Rinaldi, P., Iani, E., et al. 2024, ApJ, 969, 159
Carnall, A. C., McLure, R. J., Dunlop, J. S., & Davé, R. 2018, MNRAS,
   480, 4379
Carnall, A. C., McLure, R. J., Dunlop, J. S., et al. 2023, Natur, 619, 716
Casey, C. M., Akins, H. B., Shuntov, M., et al. 2023, ApJ, 965, 98
Castellano, M., Fontana, A., Grazian, A., et al. 2012, A&A, 540, A39
Castellano, M., Napolitano, L., Fontana, A., et al. 2024, ApJ, 972, 143
Chabrier, G. 2003, PASP, 115, 763
Chary, R., & Elbaz, D. 2001, ApJ, 556, 562
Chatzikos, M., Bianchi, S., Camilloni, F., et al. 2023, RMxAA, 59, 327
Colina, L., Crespo Gómez, A., Álvarez-Márquez, J., et al. 2023, A&A, 673, L6
Crespo, D., González-Nuevo, J., Bonavera, L., Cueli, M. M., & Casas, J. M.
   2024, A&A, 684, A109
Costantin, L., Gillman, S., Boogaard, L. A., et al. 2025, A&A, 699, A360
Curtis-Lake, E., Carniani, S., Cameron, A., et al. 2023, NatAs, 7, 622
De Rossi, M. E., Rieke, G. H., Shivaei, I., Bromm, V., & Lyu, J. 2018, ApJ,
Decarli, R., Aravena, M., Boogaard, L., et al. 2020, ApJ, 902, 110
Decarli, R., Walter, F., Gónzalez-López, J., et al. 2019, ApJ, 882, 138
D'Eugenio, F., Cameron, A. J., Scholtz, J., et al. 2025, ApJS, 277, 4
Dicken, D., Garcia Marin, M., Shivaei, I., et al. 2024, A&A, 689, A5
Draine, B. T., Aniano, G., Krause, O., et al. 2014, ApJ, 780, 172
Eddington, A. S. 1926, The Internal Constitution of the Stars (Cambridge:
   Cambridge Univ. Press)
Eisenstein, D. J., Johnson, B. D., Robertson, B., et al. 2023a, arXiv:2310.
   12340
Eisenstein, D. J., Willott, C., Alberts, S., et al. 2023b, arXiv:2306.02465
Elston, R., Rieke, G. H., & Rieke, M. J. 1988, ApJL, 331, L77
Endsley, R., Stark, D. P., Chevallard, J., & Charlot, S. 2021, MNRAS,
  500, 5229
Evans, I. N., Primini, F. A., Miller, J. B., et al. 2020, AAS Meeting, 235,
   154.05
Falcón-Barroso, J., Sánchez-Blázquez, P., Vazdekis, A., et al. 2011, A&A,
Fitzpatrick, E. L. 1999, PASP, 111, 63
Fruchter, A. S., & Hook, R. N. 2002, PASP, 114, 144
Fujimoto, S., Wang, B., Weaver, J., et al. 2024, ApJ, 977, 250
```

Furtak, L. J., Labbé, I., Zitrin, A., et al. 2024, Natur, 628, 57

```
Furtak, L. J., Zitrin, A., Plat, A., et al. 2023, ApJ, 952, 142
Galametz, A., Grazian, A., Fontana, A., et al. 2013, ApJS, 206, 10
Gandolfi, G., Rodighiero, G., Bisigello, L., et al. 2025, arXiv:2502.02637
Gardner, J. P., Mather, J. C., Abbott, R., et al. 2023, PASP, 135, 068001
Gillman, S., Smail, I., Gullberg, B., et al. 2024, A&A, 691, A299
Glikman, E., Helfand, D. J., & White, R. L. 2006, ApJ, 640, 579
González-López, J., Decarli, R., Pavesi, R., et al. 2019, ApJ, 882, 139
González-López, J., Novak, M., Decarli, R., et al. 2020, ApJ, 897, 91
Graham, J. R., & Dey, A. 1996, ApJ, 471, 720
Greene, J. E., Labbe, I., Goulding, A. D., et al. 2024, ApJ, 964, 39
Hainline, K. N., Maiolino, R., Juodžbalis, I., et al. 2025, ApJ, 979, 138
Harris, C. R., Millman, K. J., van der Walt, S. J., et al. 2020, Natur, 585, 357
Hickox, R. C., & Alexander, D. M. 2018, ARA&A, 56, 625
Iani, E., Caputi, K. I., Rinaldi, P., & Kokorev, V. I. 2022, ApJL, 940, L24
Iani, E., Caputi, K. I., Rinaldi, P., et al. 2024, ApJ, 963, 97
Ilbert, O., Arnouts, S., McCracken, H. J., et al. 2006, A&A, 457, 841
Illingworth, G. 2015, Hubble Legacy Fields ("HLF"), MAST, doi:10.17909/
   T91019
Inayoshi, K., & Ichikawa, K. 2024, ApJL, 973, L49
Indebetouw, R., Mathis, J. S., Babler, B. L., et al. 2005, ApJ, 619, 931
Jiang, L., Fan, X., Brandt, W. N., et al. 2010, Natur, 464, 380
Johnson, B. D., Leja, J., Conroy, C., & Speagle, J. S. 2021, ApJS, 254, 22
Kaspi, S., Smith, P. S., Netzer, H., et al. 2000, ApJ, 533, 631
Kennicutt, R. C., & Evans, N. J. 2012, ARA&A, 50, 531
Killi, M., Watson, D., Brammer, G., et al. 2024, A&A, 691, A52
Kirkpatrick, A., Yang, G., Le Bail, A., et al. 2023, ApJL, 959, L7
Kokorev, V., Caputi, K. I., Greene, J. E., et al. 2024, ApJ, 968, 38
Kokorev, V., Fujimoto, S., Labbe, I., et al. 2023, ApJL, 957, L7
Kriek, M., & Conroy, C. 2013, ApJL, 775, L16
Kron, R. G. 1980, ApJS, 43, 305
Kroupa, P. 2001, MNRAS, 322, 231
Labbe, I., Greene, J. E., Bezanson, R., et al. 2025, ApJ, 978, 92
Langeroodi, D., & Hjorth, J. 2023a, ApJL, 957, L27
Langeroodi, D., & Hjorth, J. 2023b, arXiv:2307.06336
Langeroodi, D., Hjorth, J., Chen, W., et al. 2023, ApJ, 957, 39
Leja, J., Carnall, A. C., Johnson, B. D., Conroy, C., & Speagle, J. S. 2019,
      J, 876, 3
Li, Y., Leja, J., Johnson, B. D., Tacchella, S., & Naidu, R. P. 2024, ApJL,
Luo, B., Brandt, W. N., Xue, Y. Q., et al. 2017, ApJS, 228, 2
Lusso, E., Comastri, A., Vignali, C., et al. 2010, A&A, 512, A34
Lyu, J., Alberts, S., Rieke, G. H., & Rujopakarn, W. 2022, ApJ, 941, 191
Lyu, J., Alberts, S., Rieke, G. H., et al. 2024, ApJ, 966, 229
Lyu, J., Rieke, G. H., & Shi, Y. 2017, ApJ, 835, 257
Maiolino, R., Uebler, H., Perna, M., et al. 2024, A&A, 687, 67
Mármol-Queraltó, E., McLure, R. J., Cullen, F., et al. 2016, MNRAS,
   460, 3587
Matthee, J., Feltre, A., Maseda, M., et al. 2022, A&A, 660, A10
Matthee, J., Mackenzie, R., Simcoe, R. A., et al. 2023, ApJ, 950, 67
Matthee, J., Naidu, R. P., Brammer, G., et al. 2024, ApJ, 963, 129
Matthee, J., Sobral, D., Darvish, B., et al. 2017, MNRAS, 472, 772
McKinney, W. 2010, in Proc. 9th Python in Science Conf., ed.
   S. van der Walt & J. Millman, 56
Meurer, G. R., Heckman, T. M., & Calzetti, D. 1999, ApJ, 521, 64
Moffat, A. F. J. 1969, A&A, 3, 455
Noll, S., Burgarella, D., Giovannoli, E., et al. 2009, A&A, 507, 1793
Oesch, P., & Magee, D. 2023, The JWST FRESCO Survey, MAST, doi:10.
   17909/GDYC-7G80
Oesch, P. A., Brammer, G., Naidu, R. P., et al. 2023, MNRAS, 525, 2864
Oke, J. B., & Gunn, J. E. 1983, ApJ, 266, 713
Osterbrock, D. E., & Ferland, G. J. 2006, Astrophysics of Gaseous Nebulae
   and Active Galactic Nuclei (2nd ed.; Sausalito, CA: Univ. Science Books)
```

Östlin, G., Pérez-González, P. G., Melinder, J., et al. 2025, A&A, 696, A57

```
Ouchi, M., Ono, Y., & Shibuya, T. 2020, ARA&A, 58, 617
Papovich, C., Cole, J. W., Yang, G., et al. 2023, ApJL, 949, L18
Pérez-González, P. G., Barro, G., Rieke, G. H., et al. 2024a, ApJ, 968, 4
Pérez-González, P. G., Gil de Paz, A., Zamorano, J., et al. 2003, MNRAS,
  338, 508
Pérez-González, P. G., Rieke, G. H., Villar, V., et al. 2008, ApJ, 675, 234
Pérez-González, P. G., Rinaldi, P., Caputi, K. I., et al. 2024b, ApJL, 969, L10
Perrin, M. D., Sivaramakrishnan, A., Lajoie, C.-P., et al. 2014, Proc. SPIE,
  9143, 91433X
Prieto-Lyon, G., Strait, V., Mason, C. A., et al. 2023, A&A, 672, A186
Ranalli, P., Comastri, A., Vignali, C., et al. 2013, A&A, 555, A42
Rieke, G. H., Alberts, S., Shivaei, I., et al. 2024, ApJ, 975, 83
Rieke, G. H., Wright, G. S., Böker, T., et al. 2015, PASP, 127, 584
Rieke, M. J., Robertson, B., Tacchella, S., et al. 2023a, Data from the JWST
   Advanced Deep Extragalactic Survey (JADES), MAST, doi:10.17909/
   8TDJ-8N28
Rieke, M. J., Robertson, B., Tacchella, S., et al. 2023b, ApJS, 269, 16
Rigby, J., Perrin, M., McElwain, M., et al. 2023, PASP, 135, 048001
Rinaldi, P., Caputi, K. I., Costantin, L., et al. 2023, ApJ, 952, 143
Rinaldi, P., Bonaventura, N., Rieke, G. H., et al. 2024, arXiv:2411.14383
Robertson, B. E., Tacchella, S., Johnson, B. D., et al. 2023, NatAs, 7, 611
Rodighiero, G., Bisigello, L., Iani, E., et al. 2023, MNRAS, 518, L19
Schlafly, E. F., & Finkbeiner, D. P. 2011, ApJ, 737, 103
Scholtz, J., Maiolino, R., D'Eugenio, F., et al. 2025, A&A, 697, A175
Schreiber, C., Elbaz, D., & Pannella, M. 2018, A&A, 609, A30
Sérsic, J. L. 1963, BAAA, 6, 41
Siebenmorgen, R., Heymann, F., & Efstathiou, A. 2015, A&A, 583, A120
Siebenmorgen, R., & Krügel, E. 2007, A&A, 461, 445
Sommovigo, L., Ferrara, A., Pallottini, A., et al. 2020, MNRAS, 497, 956
Sommovigo, L., Ferrara, A., Pallottini, A., et al. 2022, MNRAS, 513, 3122
Son, S., Kim, M., & Ho, L. C. 2023, ApJ, 953, 175
Sonnett, S., Meech, K., Jedicke, R., et al. 2013, PASP, 125, 456
Stalevski, M., Fritz, J., Baes, M., Nakos, T., & Popović, L. Č. 2012, MNRAS,
Stalevski, M., Ricci, C., Ueda, Y., et al. 2016, MNRAS, 458, 2288
Stone, C. J., Courteau, S., Cuillandre, J.-C., et al. 2023, MNRAS, 525, 6377
Sun, W., Ho, L. C., Zhuang, M.-Y., et al. 2024, ApJ, 960, 104
Tacchella, S., McClymont, W., Scholtz, J., et al. 2025, MNRAS, 540, 851
Tananbaum, H., Avni, Y., Branduardi, G., et al. 1979, ApJL, 234, L9
Taylor, M., 2011, TOPCAT: Tool for OPerations on Catalogues And Tables,
   Astrophysics Source Code Library, ascl:1101.010
Temple, M. J., Banerji, M., Hewett, P. C., Rankine, A. L., & Richards, G. T.
  2021, MNRAS, 501, 3061
The pandas development team 2025, pandas-dev/pandas: Pandas (v2.3.1),
  Zenodo, doi:10.5281/zenodo.3509134
Übler, H., Maiolino, R., Curtis-Lake, E., et al. 2023, A&A, 677, A145
van Mierlo, S. E., Caputi, K. I., Ashby, M. L. N., et al. 2024, ApJ, 966, 12
Vanden Berk, D. E., Richards, G. T., Bauer, A., et al. 2001, AJ, 122, 549
Virtanen, P., Gommers, R., Oliphant, T. E., et al. 2020, NatMe, 17, 261
Wang, B., de Graaff, A., Davies, R. L., et al. 2025, ApJ, 984, 121
Wang, B., Fujimoto, S., Labbé, I., et al. 2023, ApJL, 957, L34
Weaver, J. R., Zalesky, L., Kokorev, V., et al. 2023, ApJS, 269, 20
Whitaker, K. E., Ashas, M., Illingworth, G., et al. 2019, ApJS, 244, 16
Whitaker, K. E., Labbé, I., van Dokkum, P. G., et al. 2011, ApJ, 735, 86
Williams, C., Tacchella, S., Maseda, M., et al. 2023, Data from the JWST
  Extragalactic Medium-band Survey (JEMS), MAST, doi:10.17909/
Williams, C. C., Alberts, S., Ji, Z., et al. 2024, ApJ, 968, 34
Williams, C. C., Tacchella, S., Maseda, M. V., et al. 2023, ApJS, 268, 64
Wright, G. S., Rieke, G. H., Glasse, A., et al. 2023, PASP, 135, 048003
Wright, G. S., Wright, D., Goodson, G. B., et al. 2015, PASP, 127, 595
Yang, G., Caputi, K. I., Papovich, C., et al. 2023, ApJL, 950, L5
Yue, M., Eilers, A.-C., Ananna, T. T., et al. 2024, ApJL, 974, L26
```